

# The mechanical response of a $\alpha_2(\text{Ti}_3\text{Al}) + \gamma(\text{TiAl})$ -submicron grained $\text{Al}_2\text{O}_3$ cermet under dynamic compression: modeling and experiment

B. Amirian<sup>a</sup>, HY. Li<sup>a</sup>, J.D. Hogan<sup>a,\*</sup>

<sup>a</sup>*Department of Mechanical Engineering, The University of Alberta, Edmonton, AB T6G 2R3, Canada*

---

## Abstract

Novel experimental data, obtained using an advanced digital image correlation technique coupled to ultra-high-speed photography, have been used to develop and validate a microstructure-dependent constitutive model for a  $\alpha_2(\text{Ti}_3\text{Al}) + \gamma(\text{TiAl})$ -submicron grained  $\text{Al}_2\text{O}_3$  cermet. Utilizing experimental characterization for important simulation inputs (e.g., microstructural features size, constituent stiffness), the numerical model makes use of a variational form of the Gurson model, based on the nonlinear homogenization approach, to account for the experimentally observed deformation features in this composite (e.g., void deformation and growth, particle fracture). By considering the variability in microstructural features (e.g., particle shape, size, and aspect ratio), as well as densely packed ceramic particles, the proposed model is evaluated by comparing the numerical responses to experimental results for quasi-static and dynamic stress-strain behavior of the material. The results show that the proposed approach is able to accurately predict the mechanical response and deformation of the microstructure. Once validated, the model is expanded for studying the predominant damage mechanisms in this material, as well as determining important mechanical response features such as transitional strain rates, flow stress hardening, extensive flow softening, and energy absorbing efficiency of the material as a function of void and particle volume fraction under high strain rate loading. The totality of this work opens promising avenues for qualitative (damage micromechanisms) and quantitative (stress-strain curve) understanding of ceramic-metal composites under various loading conditions, and offer insights for designing and optimizing cermet microstructures.

*Keywords:* Microstructure-dependent constitutive model; Nonlinear homogenization approach; Dynamic uniaxial compression test; Digital image correlation; Material design

---

\*Corresponding author  
*Email addresses:* [benhour@ualberta.ca](mailto:benhour@ualberta.ca) (B. Amirian), [haoyang@ualberta.ca](mailto:haoyang@ualberta.ca) (HY. Li), [jdhogan@ualberta.ca](mailto:jdhogan@ualberta.ca) (J.D. Hogan)

## 1. Introduction

Due to its excellent corrosion resistance, high specific strength, sufficient creep resistance at elevated temperatures, and relatively low density, the two-phase titanium aluminide alloys are a potential candidate for aerospace and automotive structural applications [1, 2, 3, 4]. In comparison to their monolithic constituents,  $\gamma(\text{TiAl})$  and  $\alpha_2(\text{Ti}_3\text{Al})$ , these alloys can exhibit preferable mechanical performance as a result of containing multilayer phases with small inter-layer thickness [5, 6, 7, 8]. However, drawbacks such as poor fracture toughness and low ductility at room temperature [9, 10], and insufficient strength at high temperatures put a strict limit on their use in certain applications [11]. To remedy, introducing second phase particle reinforcements, termed intermetallic matrix composites (IMCs) can improve the toughness, creep resistance, and heat-resistance stability of the titanium aluminide material systems [12, 13, 14]. This class of ceramic-metal materials can be categorized as either metal matrix composites (MMCs) ( $\geq 50$  vol.% metal) [15, 16], or cermets ( $\geq 50$  vol.% ceramic) [17, 18]. With higher ceramic contents and associated greater strengths of cermets in comparison with MMCs, the former are expected to be far more effective as strike-face materials in aerospace and defence applications [19, 20]. In addition, ceramic-metal composites have higher fracture toughness and higher flexural strength in comparison to structural ceramics [21]. Among compatible and thermochemically stable strengthening phases for intermetallic TiAl such as SiC [22], TiB<sub>2</sub> [23], Ti<sub>2</sub>AlC [24], Ti<sub>5</sub>Si<sub>3</sub> [25], Al<sub>2</sub>O<sub>3</sub> [26], and their combination [27, 28], this paper is focused on a  $\alpha_2(\text{Ti}_3\text{Al}) + \gamma(\text{TiAl})$ -submicron grained alumina cermet due to its high temperature strength [29], excellent oxidation resistance [30], inclusive wear resistance [31], relatively low cost [32], and similarities between the coefficients of thermal expansion of the constituents [33, 34]. In addition, the submicrometer alumina grain size of the material under study here can lead to improved hardness, strength, and optical performance in comparison to the bulk alumina [35, 36, 37], which makes submicron grained advanced cermets more favourable for a wide range of applications, from light-weight ballistic armor [38] to electronic packaging substrates and medical applications [39, 40].

Researchers have developed various methods such as reactive hot processing [41], mechanical alloying [42], and sinetring process [43] for fabricating intermetallic TiAl-Al<sub>2</sub>O<sub>3</sub> to compensate for the lower ductility and fracture toughness of ceramics, as well as poor strength and stiffness of metals, when combining these two materials [44, 45]. As a result of the  $\alpha \rightarrow \gamma$  phase transformation and eutectoid reactions [8], the two-phase titanium aluminide contains a high volume fraction of lamellar grains. To date, there has been a number of published papers detailing the microstructure and mechanical properties of two-phase TiAl/Al<sub>2</sub>O<sub>3</sub> (see e.g., [26, 33, 34, 46, 47]), however, limited

studies have been devoted to the mechanical response of these unique materials under high strain rates. A limited number of research have attempted to explore the deformation mechanism of a  $\gamma$ (TiAl)-based alloys [48, 49, 50, 51], and dynamic fracture of nanograined transparent alumina [52, 53]. For example, Bertels et al. [48] confirmed the effects of superdislocations and mechanical twinning under dynamic compression loading in a  $\gamma$ TiAl-based alloy. In addition, Belenky et al. [52] showed that the dynamic initiation toughness increased significantly when compared with the quasi-static regime. Studies of Ti-based cermets under dynamic loading include dynamic mechanical damage mechanisms in TiC-1080 steel cermets [54, 55], dynamic tensile failure of 6061-T<sub>6</sub>/Al<sub>2</sub>O<sub>3</sub> [56], and the effect of confinement on impact response of TiC/Ni cermet [57]. To date, no coupled numerical and experimental studies have been investigated the dynamic mechanical behaviors (e.g., stress-strain response), microstructure parameters (e.g., inclusion shape, size, and aspect ratio), and damage mechanisms (e.g., void deformation and growth) of a intermetallic TiAl-Al<sub>2</sub>O<sub>3</sub> cermet, which are addressed in the present paper.

The mechanical properties of cermets can be predicted numerically by implementing various types of modeling approaches [58, 59, 60]. For example, Pelletier et al. [61] employed the limiting state of plastic collapse to relate the hardness of a nickel-based alloy cermet to its microstructure. Later, Engqvist et al. [62] proposed an empirical model for hardness of cemented carbides by studying the interactions between the binder and the carbide. Microstructural models such as unit cell models [63] and dislocation-based models [64] have also generated interest in predicting the strengths of cermets. For example, Legarth [65] used a unit cell approach for investigating the non-monotonical effect of a material length scale parameter on the failure strain of MMCs. In addition, the combination of continuum plasticity theory with unit cell model to study the rigid particles in ductile matrix materials was carried out by Bao et al. [66]. There are other microstructure-independent approaches, such as self-consistent models, but their usefulness are restricted to composites with a low particle volume fraction [67]. However, in some commercial cermets, the particle volume fraction can reach up to 80% [68], such that the microstructure-independent approaches are no longer valid. As a result of existing significant variability for the commercial cermets with high particle volume fraction, modeling efforts to date have focused on idealised microstructure configurations, where a limited number of studies have been made to bridge these models with experimental inputs under high strain rate loading [69, 70, 71]. For example, Ramesh and Ravichandran [72] investigated the evolution of damage and failure modes of boron carbide-aluminum cermet under dynamic loading conditions, by using the plate impact recovery technique. They found that most of the strain is accommodated by soft intermetallic phases during the initial compression pulses. Deobald and Kobayashi [73]

experimentally characterized the dynamic fracture of Si/Al<sub>2</sub>O<sub>3</sub> composites. Their study revealed an increased percentage of transgranular fracture in the dynamic fracture zone. Compton and Zok [18] described the operative damage and deformation mechanisms of TiC/Ni cermets under impact loading. Their results showed that cermets with higher toughness exhibits greater amounts of local particle cracking. The lack of understanding of the dynamic behavior and damage mechanisms of commercial cermets along with high submicron particle volume fraction motivates this jointed numerical and experimental investigations.

In the present work, an experimental setup that enables digital image correlation (DIC) measurements of the deformation field during uniaxial compressive stress state is outlined, and these experimental results are considered for numerical simulation comparisons. Scanning electron microscopy (SEM) is performed at room temperature on the fragments recovered from the uniaxial compression tests to investigate the fracture mechanisms of  $\alpha_2(\text{Ti}_3\text{Al}) + \gamma(\text{TiAl})$ -submicron grained alumina cermet under quasi-static and dynamic loading, and on the material microstructure before experiments to quantify the secondary phase alumina size and shape, and porosity in the material. To incorporate the void deformation and growth in a constitutive framework of the porous host material, a modified variational formulation of the Gurson model (MVAR) is proposed for a microstructure-based 3D face centered cubic (FCC) unit cell model with a monodisperse distribution of voids along with a polynomial cohesive zone model for decohesion of particle-matrix interface. The compression behaviors of the cermet, such as flow and compression strengths, as well as possible damage mechanisms under low and high strain rates are discussed and compared with experimental results. The influence of material microstructural variabilities (e.g., particle shapes, size, and aspect ratio), as well as particles with variability in stiffness and volume fraction are included for better simulation of true specimens under uniaxial compressive stress loading. The proposed model is shown to provide a good correspondence to the experimental data, and can serve as a fundamental approach for further material design and optimization such as increasing the confidence limits of these materials.

## 2. Material and experiments

The material investigated in this study is an  $\alpha_2(\text{Ti}_3\text{Al}) + \gamma(\text{TiAl})$ -submicron grained alumina cermet. The material is supplied by Lumiant Corporation, British Columbia, and fabricated using solid flame combustion self-propagation high-temperature sintering (SHS) process. The initial powders are aluminum (Al) and titanium dioxide (TiO<sub>2</sub>) phases to form the chemical reaction required

for obtaining the final composite. The reaction is done in the presence of metallic binder phase additives (Fe, Co, Cr, Ni, Mo, and Ni–Mo) to facilitate the densification process of the cermet [74].

### 2.1. Material characterization

100 Backscattered electron (BSE)-SEM are taken on a Zeiss Sigma field emission scanning electron microscope with the acceleration voltage (EHT) set at 20 kV and a working distance of approximately 3.8 mm (Figure 1). The lighter regions correspond to the two-phase TiAl phase because of the higher atomic number, while the darker regions are the alumina phase. By using image processing with thresholding in grayscale, the porosity level is determined as 1.2% to 3% at 2000 to 6000 times  
105 magnification, which tends to cluster around the boundary or within the alumina particle phase. The average pore size is  $0.07 \pm 0.02 \mu\text{m}$ , as measured by the major axis. The individual alumina particles appear spherical in shape and in clusters with size between  $0.5 \mu\text{m}$  to  $1.5 \mu\text{m}$  with an average of  $1 \pm 0.3 \mu\text{m}$ , and cluster sizes of  $3 \mu\text{m}$  to  $9 \mu\text{m}$ . The area fraction of the alumina phase is estimated as  $65 \pm 1\%$ . The area fraction of 65% is assumed to be equal to the particle volume fraction as  
110 an input for the simulation in the absence of volumetric data. These results from the micrographs are averaged from nine different locations randomly taken across three samples. In addition, the elastic modulus of the matrix ( $E_M = 178 \pm 31 \text{ GPa}$ ) and alumina particles ( $E_P = 278 \pm 41 \text{ GPa}$ ) are determined by nanoindentation using an ultra Nanoindentation Tester equipped with a diamond Berkovic indenter performed on an area of  $290 \mu\text{m} \times 290 \mu\text{m}$  with 900 indents in total. All the  
115 mechanical properties for the matrix and the particle are listed and discussed in Table 1 in the “Results” section.

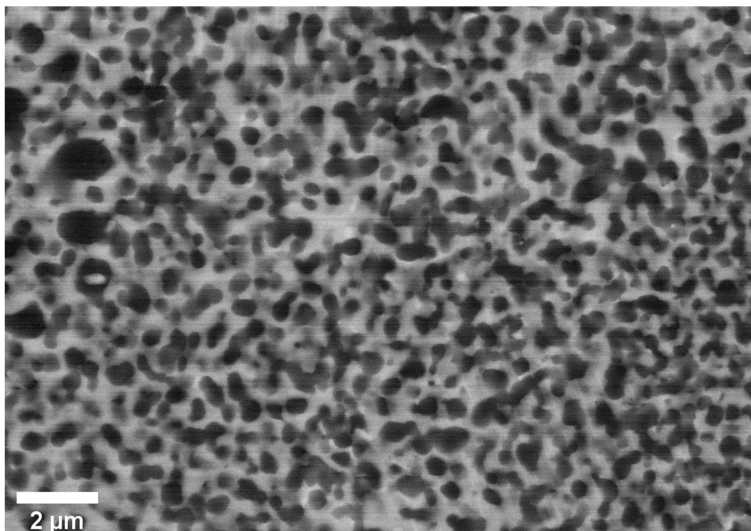


Figure 1: The experimental characterization of two-phase titanium aluminide-submicron grained alumina cermet using BSE-SEM. The black regions correspond to the alumina phase and white regions correspond to the two-phase TiAl phase.

## 2.2. Material testing

### 2.2.1. Uniaxial compression testing

Cermet tiles are cut into specimens with size of 2.3 mm (length)  $\times$  2.7 mm (width)  $\times$  3.5 mm (height) for mechanical testing. The quasi-static uniaxial compression test is detailed in Amirian et al. [75] and is briefly recounted here for completeness. The test is conducted on a standard MTS series 810 servo-hydraulic machine, and is performed under displacement control with a nominal strain rate of  $1 \times 10^{-4} \text{ s}^{-1}$ . A state of uniaxial stress is imposed on the test sample given the use of the universal testing machine in conjunction with specimen design according to literature for uniaxial stress testing [76]. In addition, high pressure grease is applied between specimen and the tungsten carbide (WC) platens to reduce frictional effect and allow free lateral expansion. Efforts are also made to avoid barreling in the specimen through the use of this lubricant, and potential barreling is investigated using high-speed camera images. In our experiments, high-speed imaging of the testing revealed no barreling, and this might be expected given the brittle nature of the cermet (i.e., failure strains are  $1.3 \pm 0.2\%$ ). A 100 kN load cell with background noise corresponding to approximately  $\pm 1 \text{ N}$  is used to record the force history during loading process. An AOS PROMON U750 high-speed camera with a full resolution of  $1280 \times 1024$  pixels is used to provide visualization on macroscopic deformation features on the specimen surface. This is coupled with the digital image correlation strain measurements using the VIC2D 6 software [77]. For these measurements, the highest quality of the brightness and contrast on the material surface is obtained by using a combination of high intensity LED with optical light guide and metallic paint. The system is adjusted so that images with good sharpness and overexposure are obtained, where an optimal subset size in the VIC2D software is achieved.

The dynamic uniaxial compression tests are conducted on a modified version of a split-Hopkinson pressure bar (SHPB) under uniaxial stress condition, where similar setups have been well documented in the literature [78, 79, 80], and the technique has been widely used on ceramics and cermets testing [78, 81]. In the current study, the SHPB equipment comprised a striker bar, an incident bar, and a transmitted bar (made from maraging steel C-350) with the length of 1016 mm and 914 mm and a common diameter of 12.7 mm for incident and transmitted bars, respectively. The signals for the stress are measured by a strain gauge mounted on the transmitted bar. The specimens are placed between two impedance matched Ti-6Al-4V titanium alloy jacketed tungsten carbide platens, where the interfaces are lubricated with extreme pressure grease to eliminate friction and allow the specimen to expand freely in the lateral dimension. The barreling effects are also checked using ultra-high-

speed video images of the failure event. No barreling is observed, and this is likely not surprising  
150 given the low failure strains in the brittle cermet in this investigation. A mild steel pulse shaper  
with a thickness of 0.0635 mm is placed in front of the incident bar (against the striker) to create a  
ramped signal profile. This specific pulse shaper provides a proper rise time ( $8 - 10 \mu\text{s}$ ) and ramp  
time for which the material can reach equilibrium state under a single pass of a loading compressive  
wave, and the natural response of the material can be captured. In this case, the total time of the  
155 whole event is within  $20 \mu\text{s}$ .

For data acquisition, an HBM Gen3i high-speed recorder from Durham Instruments is used to  
capture the voltage signals with the sampling rate at 25 MHz, and only the transmitted signal is  
used to compute the stress-time profile. An ultra-high-speed Shimadzu HPV-X2 camera is used  
to capture the failure process of the specimen during SHPB testing at 2 million frames per second  
160 with an exposure time of 200 ns. The camera has a full resolution of  $400 \times 250$  pixels, where  
128 frames can be captured at the specific frame rate. In this setup [82], a light ring equipped  
with 32 high-power LED emitters with a focal point of approximately 330.2 mm (from REL. Inc.)  
is placed concentric to the camera lens for providing further lighting to the specimen, which can  
further enhance the brightness and contrast conditions for the post-DIC analysis. Similar to quasi-  
165 static tests, DIC is used to obtain the global strain field in the dynamic tests. In these dynamic  
experiments, a K2 DistaMax lens from Infinity Photo-Optical Inc. is used to achieve a field of view  
where the full spatial resolution of the DIC analysis can be utilized. Altogether, these setups enable  
us to obtain stress-strain measurements and visualization of the surface deformation, and these are  
used to validate the model developed in this study.

### 170 **3. Constitutive modeling**

In this section, a numerical model is presented for the mechanical response of the  $\alpha_2(\text{Ti}_3\text{Al}) +$   
 $\gamma(\text{TiAl})$ -submicron grained  $\text{Al}_2\text{O}_3$  cermet under high strain rate loading. First, a porous 3D FCC  
unit cell model with four inclusions is considered for the geometry of the specimen, and the modified  
variational formulation of the Gurson model is presented for the constitutive response of the unit cell.  
175 The model has been implemented with a user-material (UMAT) fortran user-subroutine provided  
by ABAQUS/Standard. Next, the damage of matrix-particle interface is modeled by introducing a  
cohesive zone model, which was informed by deformation mechanisms observed in the experiments.

### 3.1. Geometry and model properties

Following different modeling strategies such as empirical [83] or microstructurally motivated  
180 model [59, 84], which are valid for low particle volume fraction and are described through statistical  
information, a 3D model comprising the FCC arrangement of periodic rigid particles is considered  
in this paper. This model is computationally less expensive than the geometrically realistic unit cell  
models [85], and is able to reach higher particle volume fraction (up to 73%) and local strains in the  
matrix. Moreover, the face-centered cubic structure of TiAl single crystal makes this assumption a  
185 more reasonable for geometry model of the material.

The schematic view of the arrangement of the inclusions used in the FE models is marked in  
Figure 2. The unit cell is comprised of isotropic elastic particles with a Young's modulus of  $E_P =$   
278 GPa, which is obtained from an ultra-nanoindentation tester from Anton Paar, and Poisson's  
ratio of  $\nu_P = 0.22$ . The rigid spherical particles is filled with a porous isotropic elastic-plastic matrix,  
190 with a Young's modulus and Poisson's ratio of  $E_M = 178$  GPa and  $\nu_M = 0.23$ , respectively. All  
of the related mechanical properties along with the damage parameters are given later in Table 1,  
with corresponding sources of the information. For spherical voids with a uniform monodisperse  
distribution that are constructed by means of a random sequential adsorption algorithm [86] and  
are generated by a Mathematica code, the radius of each void is:

$$R_v = L \left( \frac{3f}{4\pi N} \right)^{\frac{1}{3}}, \quad (1)$$

195 where  $L$  is the length of the unit cell,  $N$  is the number of pores in the unit cell, and  $f$  is the void  
volume fraction. The microstructure representation of cermet is also considered by ellipsoidal voids  
with unequal semi-axes. The ratios of  $L$  and pore size to the diameter of alumina phase are 1.477  
and 0.03, respectively.

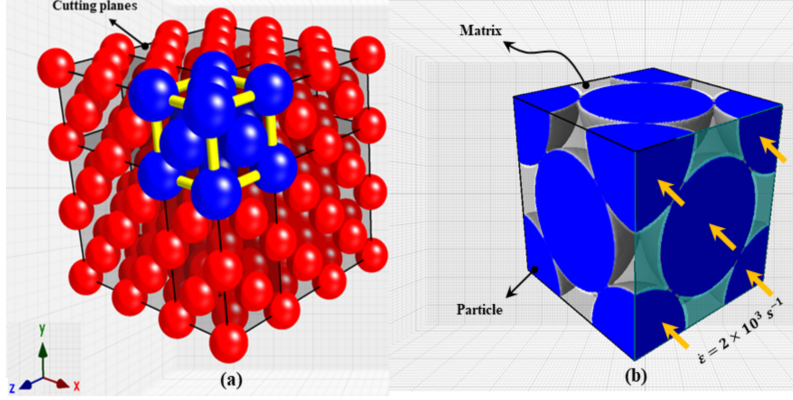


Figure 2: Sketches of the arrangement of the ceramic particles used in the FE models: (a) 3D periodic arrangements of particles, (b) 3D FCC arrangement of inclusions with the unit cell subjected to high strain rate loading.

### 3.2. The theoretical framework of $\alpha_2(\text{Ti}_3\text{Al}) + \gamma(\text{TiAl})\text{-Al}_2\text{O}_3$ cermet

200 In order to derive the constitutive equations, small strain formulation is used which is often adapted in studying brittle cermets/ceramics [71, 87]. By separating the deformation behavior of the homogenized porous material into elastic and plastic parts, the rate of deformation tensor,  $D$ , at every material point of the  $\alpha_2(\text{Ti}_3\text{Al}) + \gamma(\text{TiAl})$ -submicron grained  $\text{Al}_2\text{O}_3$  cermet is decomposed as

$$D = D^{el} + D^{pl}, \quad (2)$$

205 where  $D^{el}$  and  $D^{pl}$  are the elastic and plastic parts, respectively. As a consequence of the compressibility of the material behavior due to presence of voids, the plastic strain rate tensor is only hydrostatic.

#### 3.2.1. Elastic constitutive equations

The elastic deformation tensor of the cermet material follows the hypoelastic form as

$$D^{el} = M^e : \dot{\sigma}, \quad (3)$$

210 where  $M^e$  and  $\dot{\sigma}$  are the effective compliance tensor and Jaumann rate of the Cauchy stress, respectively. These are defined as [88]

$$M^e = M + \frac{f}{1-f} Q^{-1}, \quad \dot{\sigma} = \dot{\sigma} - \omega \cdot \sigma + \sigma \cdot \omega, \quad (4)$$

where  $\omega$  is the spin of voids relative to a fixed frame, i.e.,  $\dot{n}^i = \omega \cdot n^i$ ,  $i = 1, 2, 3$ , and  $M$  is the elastic compliance tensor of the matrix phase which is assumed to be isotropic such that

$$M_{ijkl} = \frac{1}{2\mu} K_{ijkl} + \frac{1}{3\kappa} \mathbb{J}_{ijkl}, \quad (5)$$

$$\mathbb{J}_{ijkl} = \frac{1}{3} \delta_{ij} \delta_{kl}, \quad (6)$$

$$K_{ijkl} = \mathbb{I}_{ijkl} - \mathbb{J}_{ijkl}, \quad (7)$$

$$\mathbb{I}_{ijkl} = \frac{\delta_{ik} \delta_{jl} + \delta_{il} \delta_{jk}}{2}, \quad (8)$$

$$Q_{ijkl} = E_{ijkl} : (\mathbb{I}_{ijkl} - \mathbb{S}_{ijkl}), \quad (9)$$

where  $\mu$  and  $\kappa$  denote the elastic shear and bulk moduli of the matrix,  $\delta$  and  $\mathbb{I}$  are the symmetric  
 215 second- and fourth-order identity tensors,  $f$  is the porosity,  $\mathbb{S}$  is the fourth-order Eshelby tensor [89], and  $Q$  is the microstructural fourth-order tensor which is proportional to the shear modulus, Poisson's ratio, aspect ratio of the voids, and the orientation of the ellipsoidal voids [90]. It is worth noting that the components of the effective compliance tensor depend on the void volume fraction, shape, and orientation of the voids, and these evolve in time.

### 220 3.2.2. Plasticity behavior

For obtaining the rate-dependent constitutive relations of nonlinear cermet material, the local behavior of the matrix phase is described by an isotropic, viscoplastic dissipation potential  $W(\sigma)$  as [91]

$$W(\sigma) = (1 - f) \frac{\dot{\varepsilon}_0 \sigma_{flow}}{n + 1} \left( \frac{\hat{\sigma}_e}{\sigma_{flow}(\varepsilon_M^p)} \right)^{n+1}, \quad (10)$$

where  $\sigma_{flow}$  is the flow stress of the matrix in tension which is the function of the accumulated plastic  
 225 strain  $\varepsilon_M^p$ ,  $\dot{\varepsilon}_0$  is the reference strain rate, and  $n$  is the inverse of strain rate sensitivity parameter ( $n = 1$  for linearly viscous material and  $n \rightarrow \infty$  for rate independent material response). The variational procedure, detailed in Castaneda [91], is used to derive the constitutive relations of the composite. The effective yield function can be written as [92]

$$\Phi(\sigma, s) = \frac{1}{1 - f} \sigma : m^{MVAR} : \sigma - \sigma_y^2(\bar{\varepsilon}^p), \quad (11)$$

where  $s$  is the set of internal variables and is the function of local equivalent plastic strain, porosity,  
 230 the aspect ratio of local ellipsoids, and the unit vectors in the directions of the principal axes of

the voids. The overestimation of the original variational formulation and the Gurson model for the effective response of the porous material, at high stress triaxialities and low porosity [93], is corrected by using the MVAR model. Here,  $m$  is the normalized effective viscous compliance tensor defined as [88]

$$m_{ijkl}^{MVAR} = m_{ijkl}^{VAR} + (q^2 - 1)J_{ijpq}m_{pqrs}^{VAR}J_{rskl}, \quad (12)$$

$$m_{ijkl}^{VAR} = \frac{3}{2}K_{ijkl} + \frac{3}{1-f}\mu Q_{ijkl}^{-1}|_{\nu=0.5}, \quad (13)$$

$$q = \frac{1-f}{\sqrt{f \ln(\frac{1}{f})}}, \quad (14)$$

$$Q_{ijkl}^{-1}(\mu, \nu) = \frac{1}{2\mu} \left( 15 \frac{1-\nu}{7-5\nu} K_{ijkl} + \frac{3}{2} \frac{1-\nu}{1+\nu} J_{ijkl} \right), \quad (15)$$

235 The scalar factor  $q$  preserves the convexity and smoothness of the yield surface for all the microstructural configurations. By substituting Eqs. (12-15) into Eq. (11), the yield surface is obtained as

$$\Phi(\sigma, f) = \left( 1 + \frac{2}{3}f \right) \sigma_e^2 + \frac{9}{4} \left( \frac{1-f}{\ln f} \right)^2 p^2 - (1-f)^2 \sigma_y^2 = 0, \quad (16)$$

where  $\sigma_e = \left( \frac{3}{2} \sigma^d : \sigma^d \right)^{0.5}$  is the equivalent von Mises stress,  $\sigma^d = \sigma - p\delta$  is the deviatoric part of the stress,  $p = \frac{1}{3} \sigma : I$  is the hydrostatic Cauchy stress, and  $\sigma_y$  is the yield strength of the parent phase with zero porosity. The strain hardening response of the material matrix, following the  $J_2$  flow rule, 240 is described by the yield stress as a function of the accumulated equivalent plastic strain  $\bar{\varepsilon}^p$  [88]

$$\sigma_y(\varepsilon_M^p) = \sigma_0 \left( 1 + \frac{\varepsilon_M^p}{\varepsilon_0} \right)^h, \quad \varepsilon_0 = \frac{\sigma_0}{E}. \quad (17)$$

In this expression,  $\sigma_0$  and  $\varepsilon_0$  are the initial yield stress and strain, respectively, and  $h$  is the strain hardening exponent. It is observed that in the special case of spherical voids and equaling  $f$  to zero, Eq. (16) reduces to the classic Huber-Mises model. For the strain rate sensitivity of the matrix phase, it is assumed that only the plastic deformation of the matrix leads to changes in 245 microstructure because the voids do not carry load and the elastic strains are smaller than the plastic counterpart [94]. By implementing the normality hypothesis of plasticity, consideration of the equal relation between the macroscopic plastic work and consistency condition, the plastic rate of deformation tensor is obtained as

$$\sigma : D^{pl} \equiv \dot{\lambda} \sigma : \mathbb{N} = (1-f) \sigma_y \dot{\varepsilon}^p, \quad \dot{\varepsilon}^p = \frac{\dot{\lambda} \sigma : \mathbb{N}}{(1-f) \sigma_y}, \quad (18)$$

where  $\dot{\lambda} \geq 0$  is the plastic multiplier, which can be obtained by consistency condition, and  $\mathbb{N}$  is the  
 250 direction of the plastic strain increment.

### 3.2.3. Evolution of damage

For the damage evolution, the porosity is viewed as the main damage parameter in the material. The evolution equation for porosity from the continuity equation is given by [95]

$$\dot{f} = (1 - f)D_{kk}^p + \frac{f_N}{s_N\sqrt{2\pi}} \exp \left[ \frac{-1}{2} \left( \frac{\dot{\epsilon}^p - \epsilon_N}{s_N} \right)^2 \right], \quad (19)$$

where the first and second term on the right hand side account for void growth and plastic strain controlled nucleation process, respectively.  $D_{kk}^p$  is the volumetric part of the plastic rate of deformation  
 255 tensor,  $f_N$  is the volume fraction of nucleating voids,  $s_N$  is the standard deviation of the nucleation strain, and  $\epsilon_N$  is the void nucleation strain. A critical void volume fraction is used as a fracture criteria such that the damage evolution accelerates as the damage parameter reaches to a critical value [96]. This characterizes the rapidly growing void volume fraction in the void coalescence phase.  
 260 In Eq. (19), one can use a damage rate coefficient  $K_f$ , which is defined as

$$K_f = \begin{cases} 1 & f \leq f_c, \\ \frac{f_m - f_c}{f_f - f_c} & f_c < f \leq 1, \end{cases} \quad (20)$$

where  $f_f$  is the void volume fraction at failure ( $f = f_f$ ) [97],  $f_c$  is the critical value of void volume fraction at coalescence under uniaxial tension, and  $f_m = 1/q_1$  with  $q_1$  as a constant parameter introduced by Tvergaard [98]. This function was introduced in order to account for the loss of load carrying capacity after void coalescence.

265 For implementing the local integration scheme, the integrated variables are the elastic strain tensor,  $\epsilon_e$ , the accumulated plastic strain,  $\bar{\epsilon}^p$ , and the void volume fraction. In this paper, the fully implicit method with a Newton-Raphson scheme are used for the local integration scheme, which is detailed in Amirian et al. [75]

### 3.2.4. Interface decohesion model

270 Interfaces have effects on the material design of ceramic-metal composites because of their highest responsibility for stiffness, strength, fracture behavior, and stress-bearing capacity [99, 100]. As a result of existing ceramic particles in the microstructure, debonding along the reinforcement/matrix interface is one of the main fracture micromechanisms, which is highly localized in front of the crack

tip [101].

275 There are different models for characterizing interfaces, such as a narrow region of continuum with graded properties and cohesive zones with specific traction-separation laws [102, 103]. The facilitation of numerical implementations are the major reasons for using a continuum mechanics framework rather than ad hoc methods [104], and these frameworks are commonly called *cohesive zone laws*. In this model, the traction is taken to be a function of the displacement jump across  
280 the interface, where in order to simulate the interfacial behavior of cermet, a polynomial cohesive zone model is used [105]. The normal traction ( $T_n$ ) separation ( $\delta_n$ ) relation with the assumption of  $\delta_t = 0$  is demonstrated in Figure 3.

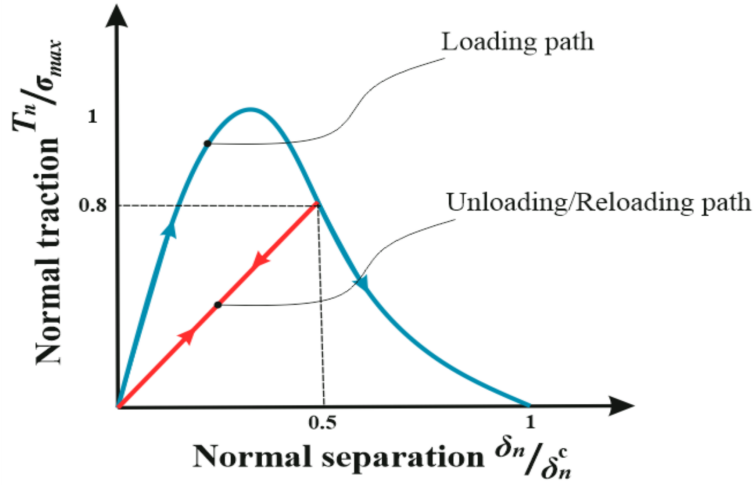


Figure 3: A traction-separation law for the polynomial cohesive zone model applied at the particle-matrix interface.

By increasing interfacial separation, the traction increases to the maximum value, which is defined as the interfacial bonding strength. After this maximum value, the traction decreases to zero where  
285 complete failure occurs. For the unloading/reloading path, the interface behavior can be evaluated by the sign of  $\Lambda$  and  $\dot{\Lambda}$  which is followed the same linear relationship. For the interface under compression, the normal and tangential traction for loading and unloading path are defined as

$$T_n = \mathbb{K} \frac{\delta_n}{\delta_n^c}, \quad \mathbb{K} > 10E_P, \quad (21)$$

$$T_t = \xi \frac{27}{4} \sigma_{max} \frac{\delta_t}{\delta_t^c} (1 - \Lambda)^2, \quad \Lambda = \Lambda_{max} < 1 \quad \text{and} \quad \dot{\Lambda} \geq 0; \quad \text{Loading path}, \quad (22)$$

$$T_t = \xi \frac{27}{4} \sigma_{max} \frac{\delta_t}{\delta_t^c} (1 - \Lambda_{max})^2, \quad \Lambda < \Lambda_{max} \quad \text{or} \quad \dot{\Lambda} < 0; \quad \text{Unloading path}, \quad (23)$$

where  $\delta_n^c$  and  $\delta_t^c$  are critical normal and tangential separation values, respectively,  $\sigma_{max}$  is the maximum normal stress of the interface,  $\xi$  is the ratio of maximum tangential strength to normal

290 strength  $\left(\frac{\tau_{max}}{\sigma_{max}}\right)$ ,  $E_P$  is the particle's stiffness, and  $\Lambda$  is the non-dimensional damage parameter which is induced from interface decohesion

$$\Lambda = \left\{ \left( \frac{|\delta_n|}{\delta_n^c} \right) + \left( \frac{|\delta_t|}{\delta_t^c} \right) \right\}^{\frac{1}{\zeta}}, \quad (24)$$

where  $\zeta$  defines the interaction of the normal and tangential separations. In the present study, an identical cohesive behavior is assumed along the normal and tangential directions ( $\xi = 1$  and  $\delta_n^c = \delta_t^c$ ) to simplify the model to capture the basic physics. In order to describe the interfacial debonding behavior, the interface fracture energy  $G$ , which is equal to the area under curve shown in Figure 3, is used [105]

$$G = \frac{9}{16} \sigma_{max} \delta_n^c. \quad (25)$$

This indicates that in purely normal separation,  $\sigma_{max}$  is the maximum traction and the total separation occurs at  $u_n = \delta_n$ . It is worth stating that only the cracking of the  $\alpha_2(\text{Ti}_3\text{Al}) + \gamma(\text{TiAl})$ -submicron grained alumina cermet is considered as the principal contributions to the interface fracture energy, and the residual strain energy released by the cracking of the reaction products along with the energy dissipated by periodic cracking of the reaction products are ignored. Next, the model is validated against the mechanical properties and failure behaviors of the experimental results.

#### 4. Results

The mechanical behavior of the  $\alpha_2(\text{Ti}_3\text{Al}) + \gamma(\text{TiAl})$ -submicron grained alumina cermet under high strain rate uniaxial compressive stress is explored using a 3D FCC unit cell model in combination with a modified variational formulation of the Gurson model. The numerical results are validated against the experimental data, and then are used to provide insights into various aspects of the material response during dynamic loading. The mechanical properties of each unit cell constituents along with the damage parameter values are given in Table 1, and will serve as reference values in the remainder of this article. The baseline for the submicron grained alumina volume fraction is 65%, and the ratio of the average pore size to the average particle size is 0.02. The quasi-static and dynamic response of the unit cell are simulated using commercial finite element software ABAQUS by implementing UMAT. For meshing the unit cell, approximately 350,000 ten-node quadratic tetrahedron elements (C3D10 in the ABAQUS FEA notation) are employed. In these simulations, the inclusions are assumed to be perfectly bonded to an elastic-plastic matrix. In

order to compare with the uniaxial quasi-static and dynamic compression tests, a fixed-displacement boundary conditions in the axial direction is implemented to one end of the unit cell, while the specimen was free to expand or contract freely in the lateral direction. The application of a fixed axial and free lateral boundary condition has been also used by Holland and McMeeking [106], Peng et al. [107], and Hu et al. [108] to simulate uniaxial compressive stress conditions. The simulations are performed by imposing a controlled displacement (uniform constant-velocity boundary condition) on the other end, with low ( $10^{-4}s^{-1}$ ) and high ( $2000s^{-1}$ ) strain rates in the axial direction, which are approximately the nominal loading rates in the experiments (shown schematically in Figure 2(b)).

Table 1: Material properties and the related damage parameters for the unit cell constituents

Parameters	Notation	Value	Reference
Young's modulus (Matrix)	$E_M$	$178 \pm 31 \text{ GPa}$	Nanoindentation test
Young's modulus (Particle)	$E_P$	$278 \pm 41 \text{ GPa}$	Nanoindentation test
Density (Matrix)	$\rho_M$	$4.1 \left(\frac{g}{cm^3}\right)$	[109]
Poisson's ratio (Matrix)	$\nu_M$	0.23	[109]
Poisson's ratio (Particle)	$\nu_P$	0.22	[110]
Yield stress (Matrix)	$\sigma_y^M$	$0.45 \text{ GPa}$	[109]
Initial yield stress (Matrix)	$\sigma_0$	$0.3 \text{ GPa}$	[88]
Strain hardening exponent (Matrix)	$N$	0.05	[75]
Initial porosity (Matrix)	$f_0$	0.01	[71]
Initial yield strain (Matrix)	$\varepsilon_0$	0.001	[71]
Specific heat (Matrix)	$C_{PM}$	$559.77 \left(\frac{J}{Kg K}\right)$	[111]
Surface energy (Particle)	$\gamma_P$	$0.97 \pm 0.04 \text{ (Jm}^{-2}\text{)}$	[112]
Interface fracture energy	$G$	$4 \text{ (Jm}^{-2}\text{)}$	[113]

#### 4.1. Quasi-static and dynamic compression behaviors

The simulated stress-strain relationships of the ceramic-metal composite compressed at low and high strain rates together with the experimental results are summarized in Figure 4. The numerical data range are obtained by changing the stiffness, shape, volume fraction, and aspect ratio of the inclusions in the unit cell structure in order to account for the variabilities of the material, and to compensate for the discrepancy between experimental and numerical results. For each of these parameters, random realizations of the properties are generated by assuming a normal distribution of the mean (values in Table 1) and a 20% uncertainty. The stress-strain data for all cases are presented as shaded regions (except for dynamic numerical loading) that represent lower and upper bounds on the stress and strain values. The different regions of the curve that correspond to the various particle shapes and porosity are noted in the caption, and this is done for ease of comparison and clarity. Figure 4(a) is discussed in the subsequent paragraph. First, the representative curves from the quasi-static and dynamic experiments are presented in Figure 4(b) in order to demonstrate

the common softening and hardening behavior in the cermet, especially for the dynamic case. As observed, the quasi-static curves (blue) tend to follow a convex behavior (values presented later when describing Figure 4(a)). For the dynamic case (red curves), the behavior is more complicated as it exhibits cycling hardening and softening behavior, which was observed in other types of cermets [55, 114, 115]. This is believed to be a consequence of a texturing phenomenon (plastic deformation) observed during dynamic loading [82]. In addition, the sensitivities of numerical stress-strain curves to inclusion shapes (prism, platelet, icosahedron, and ellipsoid) compared to experimental results is illustrated in Figure 4(c). It can be seen that the prism shape exhibits the greatest softening post-peak, while the cylinder shows a softening then hardening behavior. Overall, and as will be discussed next with respect to Figure 4(a), the numerical results reasonably capture the experimental data. The raw data is provided as supplementary to this article.

Referring back to the Figure 4(a), for the experimental data under low strain rates (red shaded region), the failure strain which is the peak strain in this case is between 1.1% and 1.4% with an average of  $1.3 \pm 0.2\%$ . The quasi-static compressive strength, which is defined as the magnitude of the peak axial stress that is sustained by the specimen, is between 2121 MPa and 2402 MPa, with an average of  $2262 \pm 141$  MPa. Strain hardening effects are observed which indicates ductility in the material when compared to, for example alumina, which behaves in a linear elastic manner until failure [116, 117]. The stress-strain curve also exhibits a yielding behavior which commences at a strength of  $\sim 1173$  MPa. For the quasi-static case, the Young's modulus of the material is between 240 GPa and 310 GPa, with an average of  $274 \pm 26$  GPa. The tangent modulus (strain hardening rate) at 0.7% strain (the cross point of numerical and experimental data) varies in the range of 109 GPa and 197 GPa, with an average of  $153 \pm 44$  GPa.

For the numerical data under quasi-static loading (gray shaded region in Figure 4(a)), 15 different realizations of the model are simulated across various void and particle concentration, and mechanical properties. Results show that high work hardening rate is maintained until about 1.4% strain. The quasi-static compressive strength is between 1970 MPa and 2578 MPa, with an average of  $2274 \pm 304$  MPa. The Young's modulus changes from 234 GPa and 282 GPa, with an average of  $258 \pm 24$  GPa. The strain hardening rate at 0.7% strain is between 87 GPa and 130 GPa, with an average of  $108.5 \pm 21.5$  GPa. For an upper limit in the elastic stiffness, the yield strength of the composite increases by 73 MPa (5% of the upper limit yield strength), and the peak stress decreases by 26.5 MPa (1% of the upper limit peak stress).

Next, the dynamic stress-strain behavior of the ceramic-metal composites are explored experimentally (brown shaded region in Figure 4(a)). The stress-strain response initially behaves as a

370 typical brittle material with a linear stress-strain curve at which time the material rapidly damages  
and there is an appreciable drop in stress, and thus, dynamic compressive strength. The dynamic  
Young’s modulus (taking the slope of the stress-strain curve at 0.1% strain) is between 240 GPa and  
270 GPa, with an average of  $255 \pm 11$  GPa. The high work hardening rate is maintained until about  
0.6% strain, after which it begins to soften or reduce near the peak stress ranged from 2696 MPa  
375 to 3447 MPa, with an average of  $3133 \pm 237$  MPa. Following this initial peak stress, there is then a  
decrease (softening) in the stress in the material until 1.1% to 1.4% strain. This initial decrease is  
then followed by an increase in stress until approximately 2% strain, after which the curve collapses  
and the material fails catastrophically.

Numerically for the high strain rate loading (hatched blue in Figure 4(a)), more than 30 different  
380 realizations in terms of particle volume fraction (60%, 65%, and 70%), Young’s modulus, and differ-  
ent void volume fraction (0.5%, 1.5%, and 3%) are simulated as a result of experimentally observed  
microstructure variabilities, as many of the alumina appears clustered in the microstructure, and  
so attempts are made for these considerations on the stress-strain response for these strain rates.  
Specifically, the numerical results for the dynamic case show that by increasing the axial strain, the  
385 stress linearly increases with slopes change from 277 GPa (region VI for platelet inclusions with 3%  
void volume fraction) to 329 GPa (region I for ellipsoid particles with 0.5% void volume fraction),  
with an average of  $303 \pm 37$  GPa (measured at 0.1% strain) until  $\sim 0.9\%$  strain. The stress-strain  
response then starts to yield until a dynamic compressive strength between 2757 MPa (at 1.1% strain  
in region VI) and 3484 MPa (at 1.6% strain in region III), with an average of  $3074 \pm 250$  MPa . The  
390  $\alpha_2(\text{Ti}_3\text{Al}) + \gamma(\text{TiAl})$ -submicron grained alumina ceramic-metal composites tend to lose their load-  
bearing capacity at strains ranging from 1.1% to 1.6%, with an average of  $1.3 \pm 0.2\%$ . The softening  
rate in this region decreases from 1.8 GPa to 1.7 GPa. As can be seen in the figure, most of the  
dynamic properties are much higher than the quasi-static compressive counterparts. For example,  
the failure strain of the composite at high strain rates is larger than that of quasi-static loading (in-  
395 creasing from 1.4% to 2.3%). For both numerical and experimental results under dynamic loading,  
the peak stress is followed by extensive flow softening, whose softening rate is less at lower strains  
and considerably high at higher strains. This softening behavior may be related to the temperature  
increase subjected to adiabatic process in dynamic loading [118]. Numerically, the growth and coa-  
lescence of microvoids plays the role of softening parameter and thus enables modeling reduction in  
400 material load bearing capacity before failure, which are detailed in the “Discussion” section.

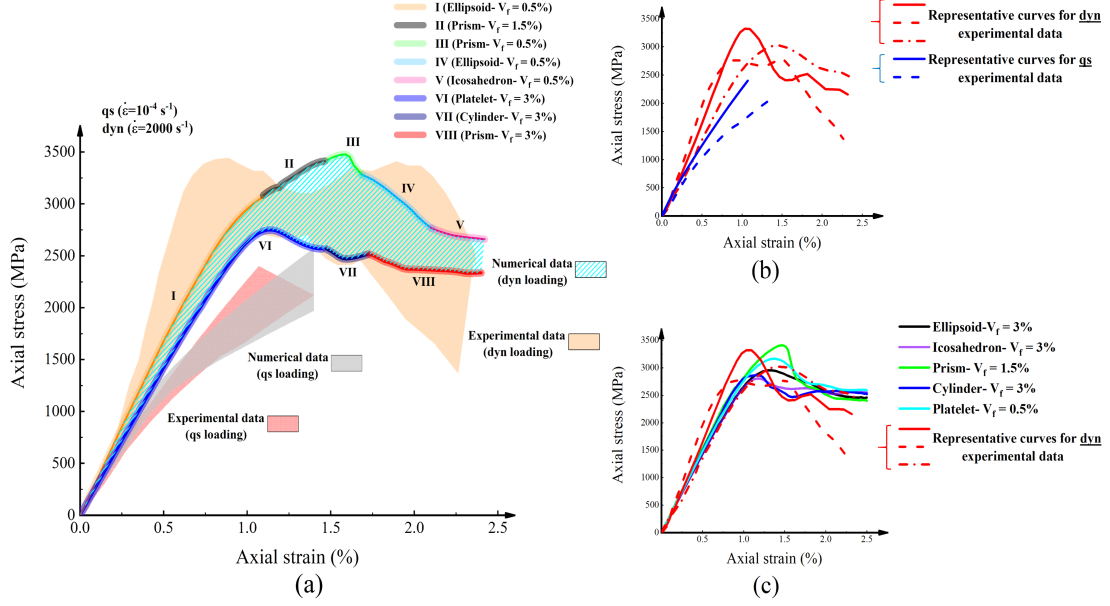


Figure 4: The mechanical response of ceramic-metal composite under uniaxial compression test: (a) the numerical and experimental axial stress vs. strain under quasi-static (qs; red- and gray-shaded region at  $1 \times 10^{-4} \text{ s}^{-1}$  strain rate) and dynamic (dyn; brown shaded region and hatched blue at  $\sim 2000 \text{ s}^{-1}$  strain rate) loading for both numerical (Num) and experimental (Exp) cases, (b) representative curves for qs and dyn experimental data, and (c) sensitivities of numerical stress-strain curves to particle shapes compared to selected experimental data.

Shown in Figure 5 is the variation of the compressive strength as a function of the strain rate. Two groups of experimental data, including some results from a previous study [75], are plotted and compared with the numerical data. The experimentally observed quasi-static compressive strengths are between 2121 MPa and 2402 MPa with an average of  $2262 \pm 141$  MPa, and the dynamic compressive strengths are between 2696 MPa and 3447 MPa with an average of  $3133 \pm 237$  MPa. It is observed that a rate dependency of compressive strength occurs. Experimentally, the dynamic compressive strength is about 1.3 times the quasi-static strength with seven order increase in strain rate. In comparison with the experimental results, the numerical compressive strength increases from 2250 MPa to 2480 MPa, with the strain rates from  $1 \times 10^{-4} \text{ s}^{-1}$  to  $800 \text{ s}^{-1}$ . Above the strain rate of  $800 \text{ s}^{-1}$ , there occurs a transition into a regime of rapid strain rate strengthening where the compressive strength increases from 2480 MPa to 5101 MPa across an increase in strain rates of  $800 \text{ s}^{-1}$  to  $3500 \text{ s}^{-1}$ . The strain rate at  $800 \text{ s}^{-1}$  is considered as the transitional strain rate ( $\dot{\epsilon}_{tr}$ ) for this material, which has been shown to be dependent on the particle volume fraction, the hardening exponent, and the strain rate sensitivity of the matrix [119]. For  $800 \text{ s}^{-1} \leq \dot{\epsilon} \leq 3500 \text{ s}^{-1}$ , the rate-dependency of the compressive strength  $\sigma_c$  is represented by a power law fit with the equation  $\sigma_c \propto \dot{\epsilon}^{0.89}$  shown in the Figure 5, which the exponent is the slope of the blue dash-dot line in this semi-log plot. The increase in rate-dependency exponent will be discussed in the context of advanced ceramics in the

“Discussion” section. According to the numerical simulations, for strain rates higher than  $3500 \text{ s}^{-1}$ , the strain rate strengthening tends to increase at a lower rate, and this can be a consequence of thermal softening or damage accumulation. The numerical results are also compared with different experimental data from the literature for single phase alumina [120, 121, 122, 123]. It shows that for high strain rate regimes, the compressive strength of the  $\alpha_2(\text{Ti}_3\text{Al}) + \gamma(\text{TiAl})$ -submicron grained alumina cermet reasonably follows the behavior of alumina inclusions.

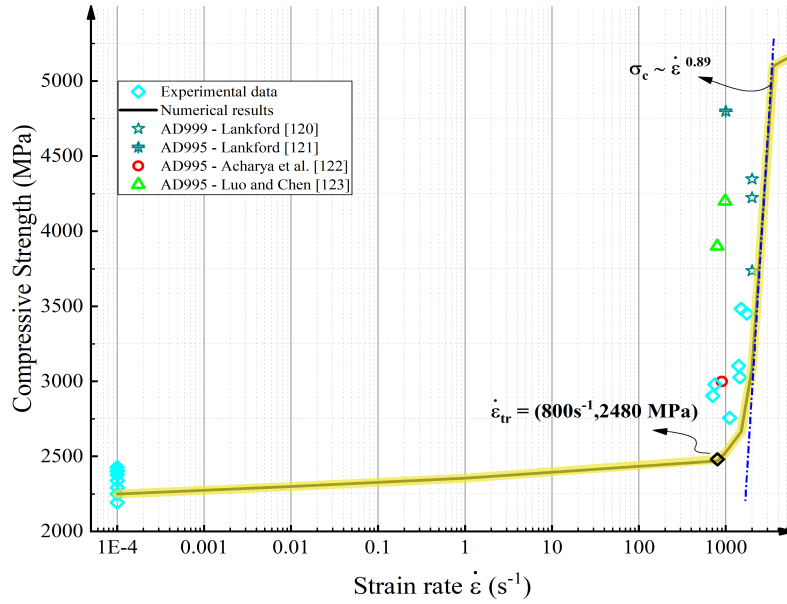


Figure 5: The change of compressive strength with strain rate, compared with experimental data. Note the logarithmic scale of the strain rate axis.

#### 4.2. Rate- and particle volume fraction dependent flow stress

Another consideration of the mechanical response of ceramic-metal composites is the variation of the flow stress for three different reinforcement volume fraction by changing the strain rates from  $10^{-4} \text{ s}^{-1}$  to  $5000 \text{ s}^{-1}$  (Figure 6). Here, the flow stress at 1.25% strain replaces the 0.2% offset flow stress commonly used in other studies, as a consequence of mitigating stress equilibrium issues at small strains during SHPB tests [48]. The experimental flow stresses at quasi-static case change from 1962 MPa to 2149 MPa. For the dynamic case ( $2000 \text{ s}^{-1}$ ), the experimentally measured flow stresses range from 2680 MPa to 3137 MPa. Numerically, it is observed that increasing the submicron grained alumina volume fraction increases the flow stress. For quasi-static case, increasing the particle volume fraction from 60% to 70% results in an increase in the flow stress by 174 MPa. While for the dynamic loading ( $2000 \text{ s}^{-1}$ ), the flow stress increases from 2956 MPa to 3088 MPa. Over the rates presented here, the flow stress at 1.25% strain for 65% particle volume fraction increases from 1900 MPa to 3200 MPa by changing the strain rates from  $10^{-4} \text{ s}^{-1}$  to  $5000 \text{ s}^{-1}$ . The strain hardening

rate for strain rates between  $100\text{ s}^{-1}$  to  $2000\text{ s}^{-1}$  is higher than its counterpart for lower strain rate value. While, for strain rates lower than  $1\text{ s}^{-1}$ , the strain hardening rate is negligible for three different particle volume fraction and the curves are nearly parallel to each other. Notable for 70% alumina concentration composite is that it begins to soften for strain rates higher than  $5000\text{ s}^{-1}$ , likely as a consequence of experiencing high concentration of damage accumulation (nucleation, growth, and coalescence of the void) which is detailed later in the paper.

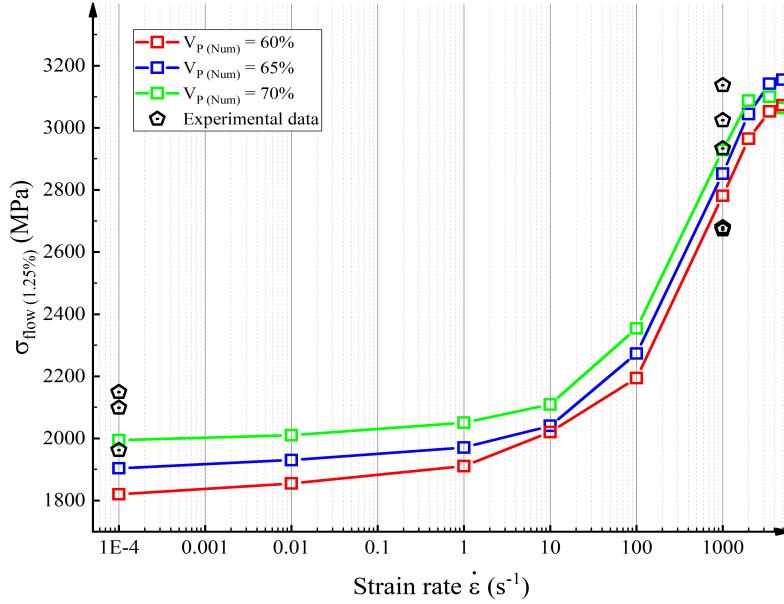


Figure 6: The variation of flow stress with strain rate at 1.25% strain considering three different particle volume fractions ( $V_P$ ), compared with the experimental data. Note the logarithmic scale of the strain rate axis.

#### 4.3. Toughening behavior under quasi-static and dynamic loading

In order to use the ceramic-metal composites in high-rate applications such as aircraft and space vehicles, understanding the toughening and energy absorption during dynamic loading is crucial towards fully realizing their potential. Experimentally, the determination of dynamic fracture toughness of cermets is complicated due to the presence of stress waves and inertial effects [124]. The effect of increasing the toughness of monolithic alloys by adding ceramic particles is investigated in this subsection by probing the effect of void volume fraction and shape on toughness. To do this, values from the dynamic stress-strain curves are utilized, which are comprised of the compressive strength (peak stress), strain to compressive strength, strain in the stress-drop zone (for strains greater than 1%), total strain, and the stress-bearing capacity, defined as the slope of the stress-strain curve in the stress-drop zone (Figure 7). The areas underneath the curve before compressive strength and beneath the stress-drop zone are called the *initiation* ( $K_{IC}^I$ ) and *propagation* ( $K_{IC}^P$ ) toughness, respectively [125].

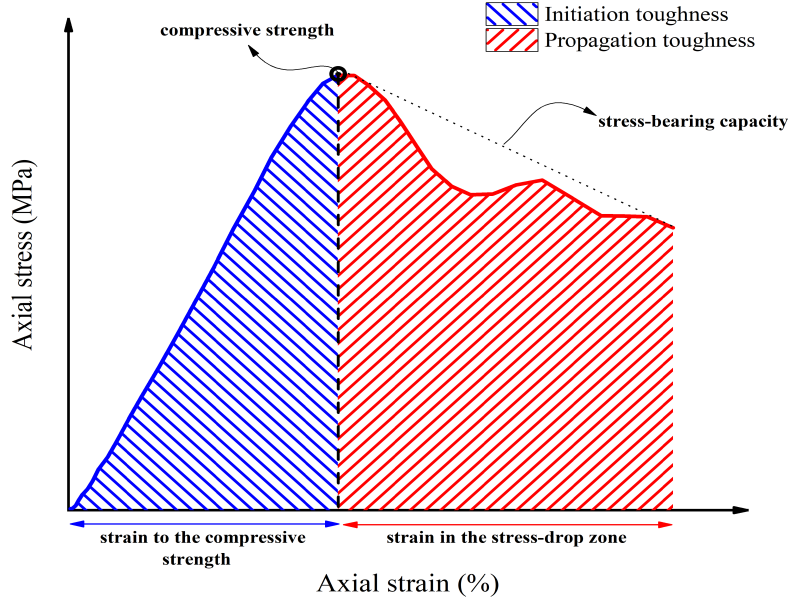


Figure 7: Schematic showing toughening behavior and its associated terms: compressive strength, strain to compressive strength, strain to stress-drop zone, stress-bearing capacity, initiation toughness, and propagation toughness.

The change of the initiation and propagation toughness with void volume fraction for different particle shapes (icosahedron, sphere, platelet, and prism) are shown in Figure 8. Higher and lower void volume fractions than are currently assessed in the material via SEM are probed to look at the sensitivity of void concentration on toughness. This is motivated by the fact that the void concentrations throughout a larger plate of the material are believed to be variable as consequence of the SHS manufacturing process. For all of the shapes, increasing the void volume fraction decreases the initiation toughness and increases the propagation toughness. The icosahedron particulate shape has the broadest range for initiation toughness (decreasing from  $31 \text{ MPa m}^{\frac{1}{2}}$  to  $18 \text{ MPa m}^{\frac{1}{2}}$  by increasing the void volume fraction from 0.5% to 3%). The lowest range is related to prismatic particles (decreasing from  $34 \text{ MPa m}^{\frac{1}{2}}$  to  $28 \text{ MPa m}^{\frac{1}{2}}$  over the strain range of zero to 1%). For the prism inclusion shapes with 0.5% void volume fraction, the energy absorbed by the specimen in the region defined for initiation toughness is the highest ( $34 \text{ MPa m}^{\frac{1}{2}}$ ). The minimum initiation toughness is for platelet inclusions with 3% void volume fraction ( $17.5 \text{ MPa m}^{\frac{1}{2}}$ ). In the case of the propagation toughness, the highest increase is related to icosahedron particles (increasing from  $24 \text{ MPa m}^{\frac{1}{2}}$  to  $31 \text{ MPa m}^{\frac{1}{2}}$  by increasing the void volume fraction from 0.5% to 3%). The prism inclusions have the lowest increase of propagation toughness (increasing from  $22 \text{ MPa m}^{\frac{1}{2}}$  to  $24 \text{ MPa m}^{\frac{1}{2}}$  by increasing the void volume fraction). The highest and lowest values for propagation toughness are related to the platelet particles with 3% void volume fraction ( $32 \text{ MPa m}^{\frac{1}{2}}$ ) and prism shapes with 0.5% void volume fraction ( $22 \text{ MPa m}^{\frac{1}{2}}$ ), respectively. The maximum total dynamic fracture toughness (de-

475 fined as the summation of initiation and propagation toughness) is for prism inclusions with 0.5%  
void volume fraction ( $56 \text{ MPa m}^{\frac{1}{2}}$ ). The main reason would be the alignment of compression loading  
with prism (angular) inclusions axes, which can serve to strengthen the microstructure under dyn-  
amic loading. The minimum total toughness ( $49 \text{ MPa m}^{\frac{1}{2}}$ ) is for platelet (polygonal) particles with  
480 the nucleation and growth of matrix voids, whereas polygonal alumina matrix voiding occurs about  
as frequently as particle fracture [121]. Together, this leads to increasing the energy absorbed by  
the microstructure. The higher fracture toughness of experimental results under dynamic loading  
( $65 \text{ MPa m}^{\frac{1}{2}}$ ) than numerical results can be related to existing metallic or glassy secondary phases  
[126, 127], which has been shown to decrease the brittleness and increase the fracture toughness of  
485 ceramic-metal materials. In addition, the transition of transgranular fracture of the ceramic parti-  
cles to intergranular fracture of the composite through the matrix phase is another explanation for  
the enhanced toughness [124]. Overall, these results demonstrate the importance of particle shape  
and void volume fraction on energy-absorption capabilities of ceramic-metal materials in damage  
tolerant design.

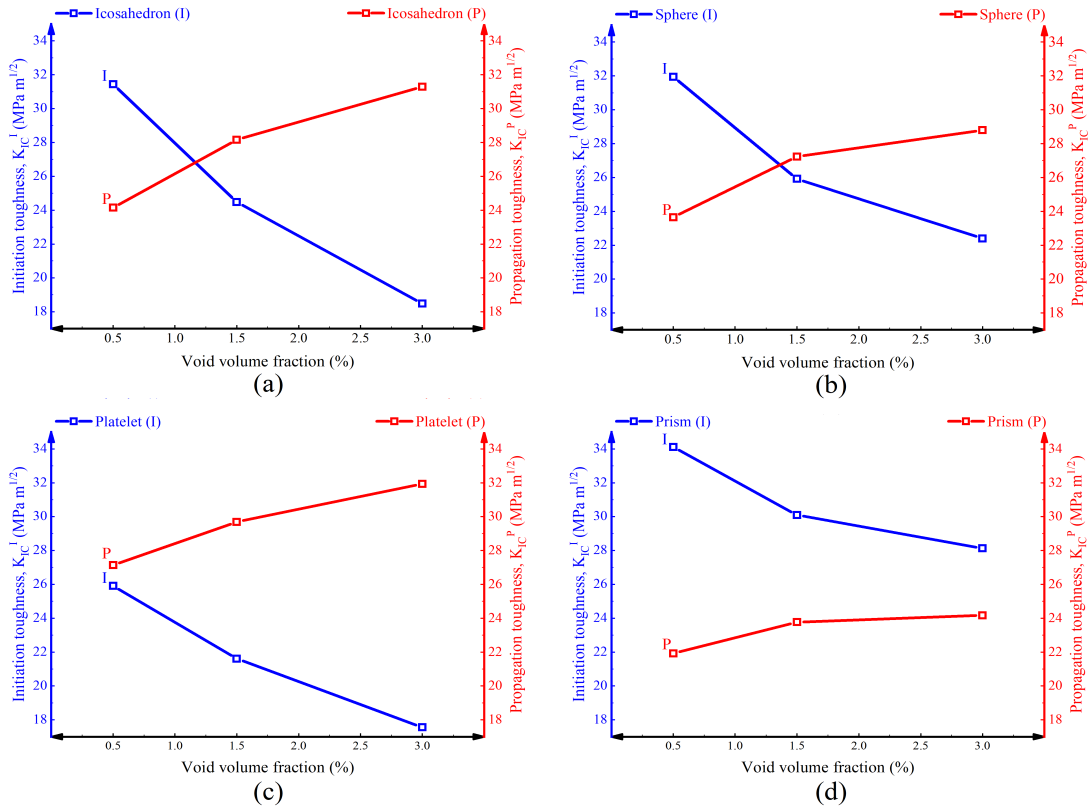


Figure 8: The change of initiation ( $K_{IC}^I$ ) and propagation ( $K_{IC}^P$ ) toughness with void volume fraction for: (a) icosahedron, (b) sphere, (c) platelet, and (d) prism inclusion shapes.

In order to examine the fracture and deformation mechanisms of the dynamically compressed  $\alpha_2(\text{Ti}_3\text{Al}) + \gamma(\text{TiAl})$ -submicron grained alumina cermet, fracture surface of the recovered fragments are investigated using SEM, and these are compared with the contour of equivalent von Mises stress from the numerical simulation (Figure 9). Shown in Figure 9(a) is the FESEM micrograph taken on the fracture surface obtained from one of the recovered fragment in a dynamic experiment for postmortem analysis and characterization of microscopic failure. The overall failure is a combination of intergranular fracture through the matrix and transgranular fracture inside the submicron grained alumina phase. The crack is observed to start from the top left corner (sufficiently high local stress concentration at the particle-particle contact points), and this appears to propagate along the alumina particles and through the titanium aluminide matrix. There is also evidence of particle pull-out followed by particle cracking along the crack path. Shown in Figure 9(b) is a magnified view on one of the fracture sites of alumina particles. It is observed that a transgranular fracture through the alumina particle occurs, where its neighbor particles remained intact. To compare these particle cracking mechanisms, a plot of the equivalent von Mises stress in the FCC unit cell is shown in Figure 9(c). For the numerical simulations, the icosahedron (20 face polyhedron with aspect ratio of 1, sphericity of  $\approx 0.94$ , and volume fraction of 65%) shape is considered for the reinforcements to capture the real shape of particles observed in the composite at this scale. It is observed that the crack spans from one corner of polygonal alumina particle, which is limited by the matrix and other particles, and it passes to the upper particle (on planes parallel to the compressive loading axis) until it is arrested by the ductile matrix. It is also observed that the stress state is spatially very heterogeneous, and there exist regions wherein the von Mises stress is positive (tensile stresses) within the matrix. These localized tensile stresses result in the dilation of the matrix. Generally, the fracture behaviors of the material captured by using the 3D unit cell model under dynamic compression loading is in good agreement with the experimental observations. The stress analysis on cracked particle as a result of internal effects induced by rapid loading is studied later in “Discussion” section.

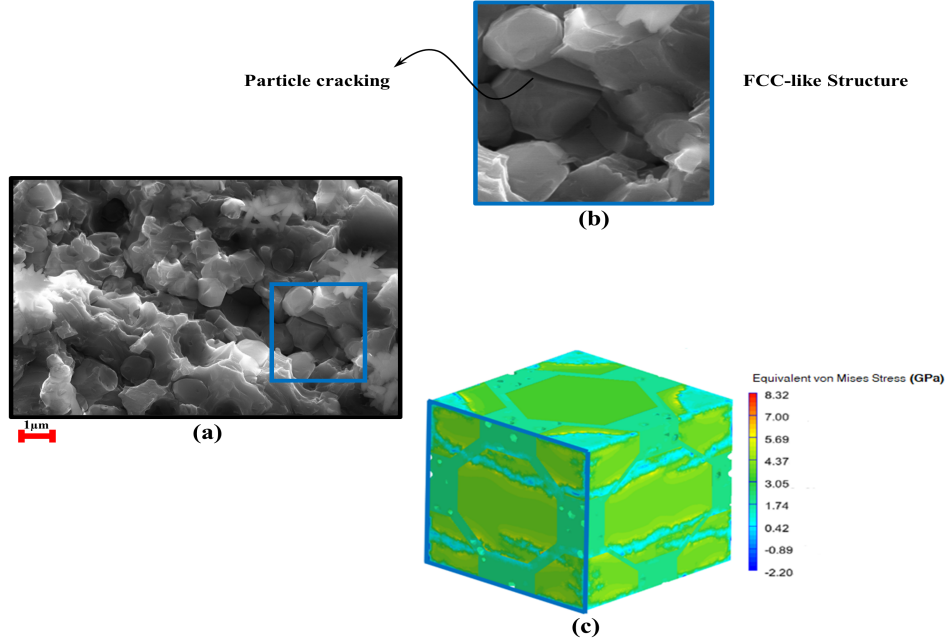


Figure 9: The fracture mechanism (particle cracking) of dynamically compressed composites: (a) SEM image of the fracture surface, (b) the magnified region with FCC-like structure comprised of particle cracking, and (c) contours of equivalent von Mises stress demonstrating fracture pattern through the alumina particle.

As a result of having a porous matrix (void volume fraction of  $1.5 \pm 1\%$ ), the other fracture phenomenon in this type of cermet is the deformation of two-phase TiAl matrix via the growth and coalescence of voids, which is explored in Figure 10. Shown in Figure 10(a) is the SEM image demonstrating internal ductile void growth and coalescence in a dynamically compressed fragment. In the image, it is observed that the crack has a high tendency to initiate from the existing voids and propagate through the neighboring voids, leading to softening behavior (loss of load-bearing capacity) of the cermet. In the magnified image in Figure 10(b), a void can be seen on the crack path, where its orientation coincides with the likely stress concentration point leading to fracture initiation and growth. The experimental observations are compared with simulation results of void growth around particles (Figure 10(c)) for various strain evolution (Figure (10d)). The failure criterion in the simulation is modeled by the modified variational formulation of the Gurson model, which incorporates the void deformation and growth after large deformation, as the damage parameter reaches to a critical value. For the simulation results, the void with an ellipsoid geometry and aspect ratio of 1 with the ratio of void to particle size changing from 0.02 to 0.04 is used, and a mesh sensitivity analysis is performed to ensure no mesh size dependence of the results. In these simulations, the initial void volume fraction is considered to be 0.1%, and this is determined from SEM images on as-received (undeformed) materials. The contours of axial strain in the loading direction at different total engineering strains of 0.5%, 1%, 1.25%, 1.5%, 2%, and 2.25% are given

535 in Figure 10(d). It is observed that strains begin to accumulate for selected voids for strains lower than the yield (0.5% strain) in the loading direction, and these evolve and connect adjacent voids, which are close to the particle by 1% strain. After coalescence (1.25% strain), additional voids begin to accumulate strain (1.5% strain), and the strain fields from these voids eventually coalesce with neighboring voids (2% strain). The complete coalescence (2.25% strain) coincides with an increase  
 540 in global strain. It is worth noting that voids tend to grow toward the particle-matrix interface until it is arrested at the free edges. In addition, the positive heterogeneous total strain (tensile strain) shows dilation in the matrix. As can be seen, void growth behavior qualitatively match with that observed experimentally.

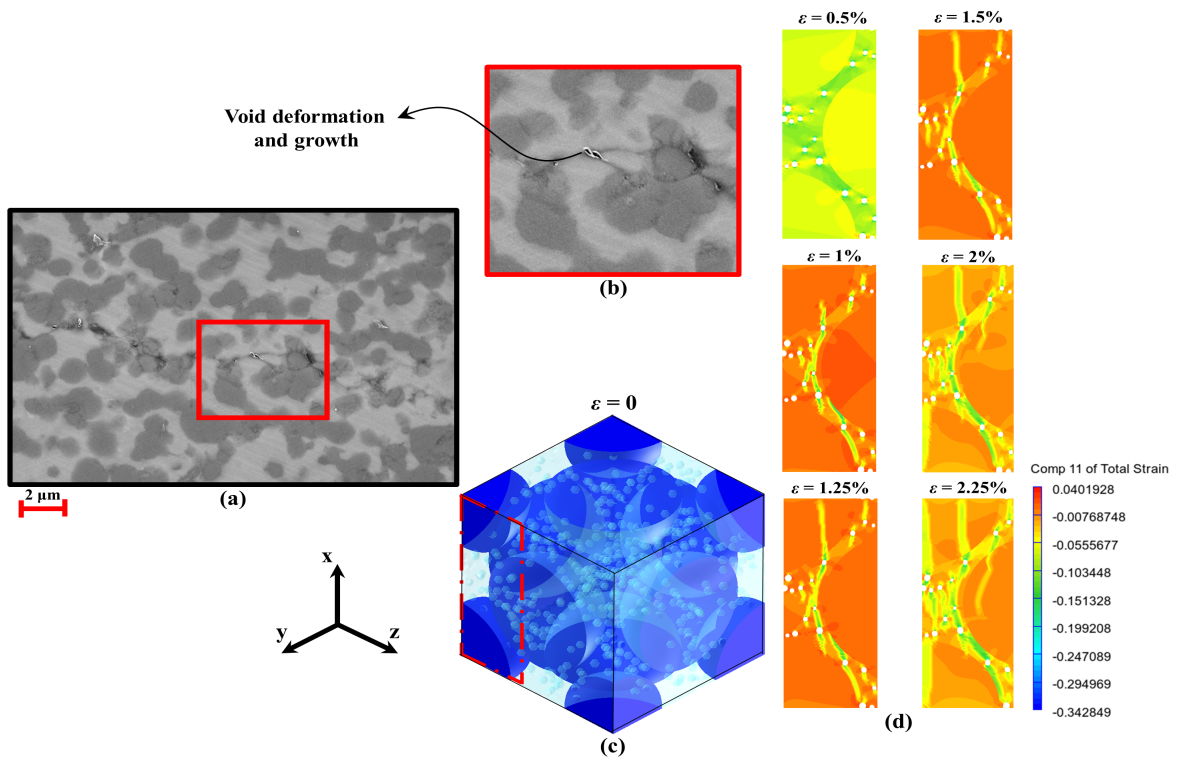


Figure 10: The fracture mechanism (void growth) of dynamically compressed  $\alpha_2(\text{Ti}_3\text{Al}) + \gamma(\text{TiAl})$ -submicron grained alumina cermet: (a) SEM image of the polished fracture surface, (b) close-up observation of the framed area in (a) including void deformation and growth, and (c) 3D unit cell with porous matrix along with contours of compressive total strains at  $\varepsilon = 0.5\%$ ,  $\varepsilon = 1\%$ ,  $\varepsilon = 1.25\%$ ,  $\varepsilon = 1.5\%$ ,  $\varepsilon = 2\%$ , and  $\varepsilon = 2.25\%$ .

Finally, interfacial debonding damage is numerically investigated by using the polynomial cohesive zone model and compared with the experimental results. The SEM images along with contour  
 545 mapping of equivalent plastic strain in the unit cell are illustrated in Figure 11. Figures 11(a) and 11(b) are micrographs taken on the fracture surfaces showing the interfacial debonding mechanisms. As can be seen, the debonding can happen in both the matrix-particle and particle-particle interfaces. The propensity of these two debonding mechanisms is hard to quantify, but it is postulated

550 that the density of the matrix-particle debonding will be higher due to less amount of energy needed to break apart the titanium aluminide-alumina interface. It is observed that the top and bottom boundaries of the particle are separated from the matrix during loading (Figure 11(b)). The numerical comparisons are shown in Figures 11(c) and 11(d), in which the former shows the arrangement of the particles and voids in the FCC unit cell, and the latter demonstrates equivalent plastic strain contours and associated particle debonding (indicated with arrows). For the numerical model, the interface fracture energy and the plane strain Young's modulus of  $\alpha_2(\text{Ti}_3\text{Al}) + \gamma(\text{TiAl}) - \text{Al}_2\text{O}_3$  are assumed to be about  $4 \text{ Jm}^{-2}$  and 180 GPa, respectively [113]. According to Figure 11(d), at small strain ( $\varepsilon = 0.5\%$ ), a small debond is found along the lower interface of the middle particle. By increasing the strain ( $\varepsilon = 0.7\%$ ), the upper interface of the particle starts to debonding. A further increase in applied strain ( $\varepsilon = 0.9\%$ ) leads to additional particle decohesion, and the strain distribution becomes heterogeneous. At the final stage ( $\varepsilon = 1.3\%$ ), debonding begins to propagate from left to right along the interface, and the debond arrest occurs at the location of around  $45^\circ$  from the compression axis. Similar behavior has been shown for rate-dependent interfacial debonding of MMCs by Zhang et al. [128]. Also, the maximum equivalent plastic strain seems to happen at two adjacent voids between the particle and the boundary edge in the loading direction. The comparisons between experimental observation and numerical result are found to be reasonable.

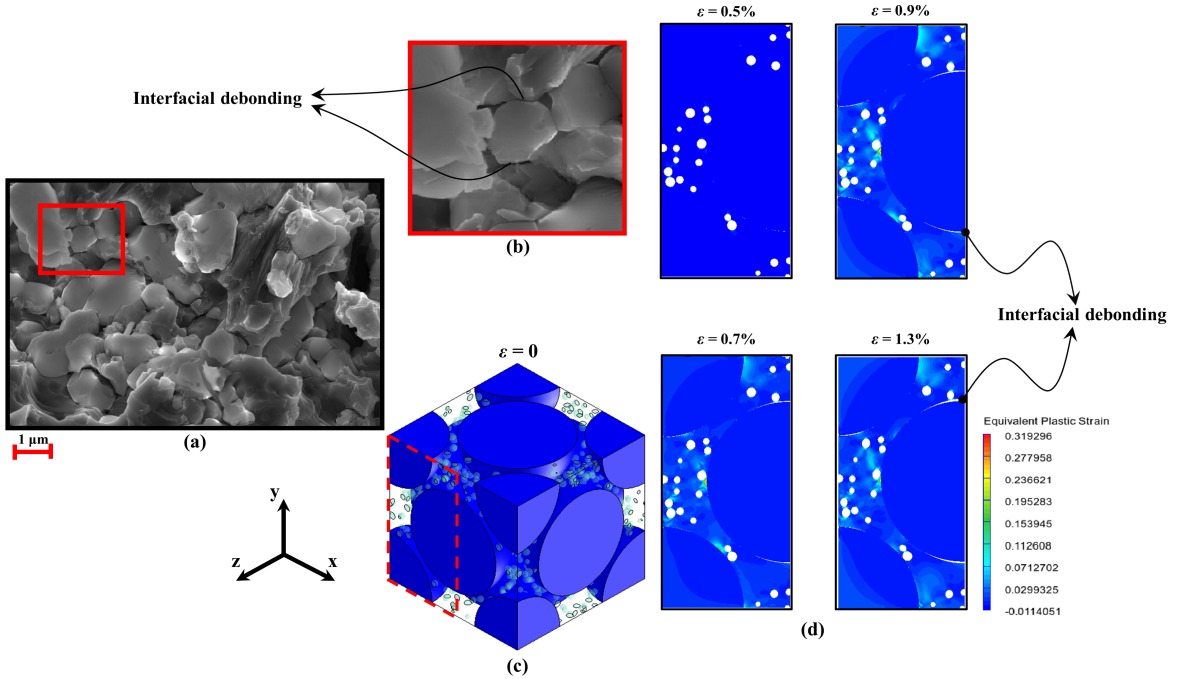


Figure 11: The fracture mechanism (interface debonding) of dynamically compressed  $\alpha_2(\text{Ti}_3\text{Al}) + \gamma(\text{TiAl})$ -submicron grained alumina cermet: (a) SEM image of the fracture surface, (b) the magnified region with FCC-like structure comprised of interfacial debonding, and (c) 3D unit cell with porous matrix along with (d) contours of the equivalent plastic strain at  $\varepsilon = 0.5\%$ ,  $\varepsilon = 0.7\%$ ,  $\varepsilon = 0.9\%$ , and  $\varepsilon = 1.3\%$ .

## 5. Discussion

In this study, a modeling framework was developed to predict the mechanical behavior of a  $\alpha_2(\text{Ti}_3\text{Al}) + \gamma(\text{TiAl})$ -submicron grained alumina cermet under low ( $1 \times 10^{-4} \text{s}^{-1}$ ) and high (up to  $5000 \text{s}^{-1}$ ) strain rate uniaxial compressive stress loading. A modified variational formulation of the Gurson model was employed to a 3D FCC unit cell for an elastic-plastic porous matrix, and three main damage mechanisms were studied and then validated with experimental results obtained from quasi-static and dynamic uniaxial compression tests: 1. particle cracking, 2. void deformation and growth, and 3. interface decohesion. The previous works on quasi-static and dynamic behavior of MMCs and idealised cermets with low reinforcement volume fraction and pore-free matrix [69, 129, 130] have been expanded both numerically and experimentally. Material characterization was carried out using SEM scans in order to generate microstructural inputs into the proposed model, and the experimental stress-strain responses were obtained from a novel DIC technique coupled to high-speed imaging and uniaxial compression experiments. Altogether, this study can give insights for designing and implementing of ceramic-metal composites in reliable structures. In the following sections, the results are summarized and implications are presented.

### 5.1. The investigation of material response under quasi-static and dynamic loading conditions

The experimental and numerical stress-strain behavior of the  $\alpha_2(\text{Ti}_3\text{Al}) + \gamma(\text{TiAl})$ -submicron grained alumina cermet under uniaxial compression in quasi-static and dynamic loading were first compared in Figure 4. The high strain rates obtained from the SHPB experiments were in the range of  $1100 \text{s}^{-1}$  to  $2000 \text{s}^{-1}$ . By taking the slope of the experimental (numerical) stress-strain curve at 0.1% strain, the average quasi-static and dynamic stiffnesses were  $274 \pm 26 \text{ GPa}$  and  $255 \pm 11 \text{ GPa}$  ( $258 \pm 24 \text{ GPa}$  and  $303 \pm 37 \text{ GPa}$ ), respectively. The increasing trend in stress-strain behavior was maintained until about 0.7% and 1.4% strain for high and low strain rates, respectively. In both the experimental and numerical cases, the initial behavior of the material was the same as typical brittle material with a linear stress-strain behavior. The difference between the stress in the material for the experimental and numerical results (from 0.1% to 0.9% strain) can be attributed to particle clustering in the specimen that was observed in SEM images (Figure 1), and was not accounted for explicitly in the unit cell model (schematic in Figure 2). This experimentally observed particle agglomeration leads to increasing the plastic strains accumulated in the matrix, higher strain hardening, and thus a higher flow stress. For the quasi-static case, there is also likely some degree of porosity in the actual material along with assuming uniform and homogeneous distribution of alumina submicron particles

in the model, resulting in higher numerical stress-strain values as compared with the experimental data [131]. Additionally, the generation, pinning down, and accumulating dislocations within the grain, and existing precipitates in the grain interior is another reason for higher strengths value of experimental than numerical results in that region [132].

After the linear region, the stress in the material starts to yield until reaching to the peak stress. The higher stress-strain values of experimental data under dynamic loading in comparison with numerical results in the stress-drop zone can be related to the limited number of reinforcements used in the unit cell model. The compressive strength and failure strain were around 1.3 times the values obtained from quasi-static tests with a seven order increase in strain rate from  $10^{-4} \text{ s}^{-1}$  to  $2000 \text{ s}^{-1}$ . After the peak stress, the strain hardening effect of plastic deformation was quickly accompanied by the flow softening behavior of the material. One reason is increased damage formation and accumulation processes, which was experimentally and numerically initiated at 0.9% and 1.3% strain, respectively. The other potential reason is related to prolific banding and associate surface rumpling within the matrix, as observed experimentally by Longy and Cagnoux [133].

## 5.2. The effect of adiabatic thermal softening

Under high strain rate loading, thermal softening due to the work exerted on the matrix can be one of the reasons for the flow softening behavior after the peak stress in stress-strain curve, which can be evaluated under an adiabatic assumption as [118]

$$\Delta T = \frac{0.95\eta}{\rho_M C_{pM}} \int_0^\varepsilon \sigma d\varepsilon, \quad (26)$$

where  $\rho_M$  is the density of the material,  $C_{pM}$  is the specific heat, and  $\eta$  is the thermal efficiency that is given by [134]:

$$\eta = \begin{cases} 0 & \dot{\varepsilon} \leq 10^{-3} \text{ s}^{-1}, \\ 0.316 \log \dot{\varepsilon} + 0.95 & 10^{-3} \text{ s}^{-1} < \dot{\varepsilon} < 1.0 \text{ s}^{-1}, \\ 0.95 & \dot{\varepsilon} \geq 1.0 \text{ s}^{-1} \end{cases} \quad (27)$$

In this study, the potential temperature increase is explored as a consequence of existing flow softening in the numerical and experimental results. By substituting the related parameters from Table 1 into Eq. (26), the average temperature increase under dynamic loading is around  $25^\circ \text{ K}$ , which is lower than the melting point of the matrix. An adiabatic temperature rise about  $20^\circ \text{ K}$  for 60 %  $\text{TiB}_2/\text{Al}$  composite and less than  $5^\circ \text{ K}$  for 55 %  $\text{Al}_2\text{O}_3/\text{Al}$  have been previously reported [135, 115].

From this analysis, these low global temperature increases are not believed to play roles in the experimentally and numerically flow softening behavior of the cermet. However, there still may be  
625 localize temperature rises in the narrow region of ceramic-metal interfaces, which were not captured in the simulations or observed in the SEM analysis. This highly localized temperature increase occurs as a result of lower thermal conductivity for alumina nanoparticles ( $22 \text{ Wm}^{-1}\text{K}^{-1}$ ) than that of two-phase TiAl ( $35 \text{ Wm}^{-1}\text{K}^{-1}$ ). In addition, the highly non-uniform local strain rate distribution in the matrix due to constraining effects from particles, along with rapid sliding of particles under  
630 high strain rates, may result in softening or even melting of the low melting point matrix [136, 137].

### 5.3. Strain rate effects on compressive strength

The compressive strength of the cermet for quasi-static and dynamic strain rates was studied both numerically and experimentally, and then compared with different alumina materials from the literature (Figure 5). Unlike experimental data which were carried out for only two strain rate  
635 regimes, the numerical method was able to investigate the material response under intermediate strain rates and rates slightly greater than those achievable in the SHPB tests. Experimentally, the quasi-static compressive strength were between 2121 MPa and 2402 MPa with an average of  $2262 \pm 141$  MPa. While for the dynamic case, the dynamic compressive strength was between 2696 MPa and 3447 MPa with an average of  $3133 \pm 237$  MPa. The experimental compression strength  
640 increases from 2402 MPa to 2696 MPa with a seven order increase in strain rates in the minimum case. In the maximum case, increasing the strain rate lead to varying the compressive strength from 2121 MPa to 3447 MPa. In addition, the experimental failure strain increases from 1.1% to 2.3% with increasing strain rates from quasi-static to dynamic loading ranges. Numerically, increasing the strain rate from  $1 \times 10^{-4} \text{ s}^{-1}$  to  $800 \text{ s}^{-1}$  leads to increasing the compressive strength of the material by  
645 10% (from 2250 MPa to 2480 MPa). For high strain rate regimes ranging from  $800 \text{ s}^{-1}$  to  $3500 \text{ s}^{-1}$ , a 106% increase in compressive strength was observed over these rates (from 2480 MPa to 5101 MPa). For this  $\alpha_2(\text{Ti}_3\text{Al}) + \gamma(\text{TiAl})$ -submicron grained alumina cermet, the critical strain rates was about  $\dot{\epsilon} \simeq 800 \text{ s}^{-1}$ , above which a rapid transition occurred into a high strain rate strengthening regime. Differences in the rate effects between the experiments and numerical model may be attributed to  
650 additional porosity [138] that likely exists in the material due to the particle clustering that is not captured in the model. For strain rates lower than the transitional value, the matrix material dictates the strain rate sensitivity (0.02 for two-phase titanium aluminide [109]) of the compressive strength, which is controlled by the thermally-activated growth of microcracks. For higher strain rates value, the constraining effect of the particles can result in increasing the local strain rate near the inclusion-

655 matrix interface, and pushes the composite into the high strain rate regime [119]. For  $\alpha_2(\text{Ti}_3\text{Al}) + \gamma(\text{TiAl})$ -submicron grained alumina cermet under dynamic loading, the strain rate exponent was found to be 0.89 in excess of the cube-root theoretical maximum for brittle materials. By using the model of Paliwal and Ramesh [139], the strain rate sensitivity exponent was found to be closer to 2/3 for advanced ceramics, and was considered as a scaling model for the compressive strength  
660 of brittle materials [140]. For experimental studies on hot-pressed silicon nitride and pyroceramic matrix reinforced with SiC, the strain rate exponents were 0.87 and 0.77, respectively [141]. A reason for this high strain rate exponent has been related to the possibility of kink nucleation and propagation by cermet with high particle volume fraction which involves very high local strain rates [141]. Additionally, a strain rate exponent higher than 0.33 implies that the consequence of increasing  
665 strain rate must be to involve crack initiation as well as crack propagation, which may manifest itself through rate-dependent localized plasticity [142]. This local plastic flow can be suppressed by high loading rates, thereby inhibiting dislocation-nucleated microfracture and increasing the strength rapidly [143].

#### 5.4. The study of flow stress of the $\alpha_2(\text{Ti}_3\text{Al}) + \gamma(\text{TiAl})$ -submicron grained alumina cermet

670 In this paper, the effect of different particle volume fractions (60%, 65%, and 70%) on the rate-dependent flow stress in the material taken at 1.25% strain was also investigated (Figure 6). The experimental quasi-static flow stress was between 1962 MPa and 2149 MPa. Under dynamic loading ( $2000\text{ s}^{-1}$ ), the experimentally measured flow stress ranged from 2680 MPa to 3137 MPa. The proposed numerical model was used to evaluate the flow stress for strain rates up to  $5000\text{ s}^{-1}$ .  
675 The numerical flow stress varied from 1820 MPa to 1994 MPa for low strain rates loading. While for high strain rates loading ( $1000\text{ s}^{-1}$ ), the numerical flow stress ranged from 2781 MPa to 2928 MPa. For this part of the study, the numerical results were reasonably captured the experimental data. At higher strain rates for highest particle volume fraction, the stress softening rate was more significant than the other cases due to relatively shorter deformation times. By increasing the strain rates, it has  
680 been shown that the presence of high volume fraction of ceramic submicron particles in ceramic-metal composites increases the flow stress as a consequence of stronger constraining effect of the particles [144]. In addition, Zhu et al. [136] investigated that high particle content composites form a network structure whereby the external load can be transferred directly via particles, results in higher flow stress. For cermets with particle volume fractions higher than 70%, where the interparticle spacing  
685 is much smaller than average, the structure becomes unstable and collapse by particle sliding as a result of existing tangential stress between adjacent particles [145]. Moreover, the adiabatic heating

generated from the work hardening process promotes the occurrence of dynamic recrystallization, which leads to rapidly decrease of flow stress with the continuous increase of strain rate [146]. On the other hand, the small size alumina inclusions can increase the resistance to crack propagation by reducing the size of the nucleating flaws. This refined microstructure plays an important role as barriers to the enablement and transmission of dislocations [132], matrix hardening by geometrically necessary dislocations, and channeled plastic flow in the matrix between particles [147]. In other words, the Orowan strengthening, which results from the interaction between dislocations and the highly-dispersed reinforcement, becomes favorable in the materials [148].

To study the flow stress of the material in terms of strain rate sensitivity (SRS), the corresponding relation is often used [149]

$$SRS = \frac{\sigma_{fd} - \sigma_{fq}}{\sigma_{fq}} \frac{1}{\ln(\frac{\dot{\epsilon}_d}{\dot{\epsilon}_q})}, \quad (28)$$

where  $\sigma_{fq}$  and  $\sigma_{fd}$  are the quasi-static ( $1 \times 10^{-4} \text{ s}^{-1}$ ) and dynamic ( $2000 \text{ s}^{-1}$ ) flow stress at a constant plastic strain. By taking the flow stress at 1.25% strain, the results showed an increase of the SRS from 0.005 ( $1 \times 10^{-4} \text{ s}^{-1}$ ) to 0.04 ( $2000 \text{ s}^{-1}$ ). The reported strain rate sensitivities for  $\text{Al}_2\text{O}_3/\text{Al}$ ,  $\text{B}_4\text{C}/\text{Al}$ , and  $\text{TiB}_2/2024\text{Al}$  composites were in the range of 0.02 to 0.05 [150, 151]. A strain rate sensitivity ranging from 0.02 to 0.04 (at 1.25%) was obtained from experimental data in this study, which has been shown to be controlled by the sensitivity of the matrix and the interaction of particles and matrix [119]. The variation of experimental SRS can be related to a material microstructural variabilities related to the coupling of the strain rate sensitivity of the matrix and the constraining effect of the particles, which is stronger when the applied strain rate is higher or the particle volume fraction is larger. In addition, the stress distributed through the particles increases as the strain rate increases under dynamic loading, which enhances the SRS of the composite [152].

### 5.5. The micromechanisms of internal damages

The theoretical models for analyzing particle cracking, matrix void-induced damage, and interface debonding have been developed for MMCs material under low and high applied strain rates [153, 154, 155], however, the experimental data are lacking between the low and high strain rate regimes for ceramic-metal composites with high particle volume fractions. Limited studies involving the modeling of ceramic-metal composites have considered rate effects, different damage mechanisms, and real microstructural variables which are addressed in the present work. Among the different damage modes present in particle-reinforced ceramic-metal composites, particle fracture is

commonly encountered for composites containing brittle reinforcements that are strongly bonded to a tough matrix (Figure 9). To further analyze particle fracture results in this study, this sub-section investigates the fracture stress on the submicron alumina inclusions.

Particle cracking by propagation of an internal defect is given by the Griffith equation [156]:

$$\sigma_p = \left( \frac{2E_P\gamma_P}{\pi C} \right)^{0.5}, \quad (29)$$

720 where  $\sigma_p$  is the stress on the particle,  $\gamma_P$  is the particle fracture surface energy,  $E_P$  is the Young modulus of particle, and  $C$  is the internal crack length. By substituting the related values from Table 1 into Eq. (29), considering the crack length equal to  $1 \mu m$ , it can be calculated that the stress on the particle is about 440 MPa under dynamic loading. This is deemed to be comparable with the scale provided in Figure 9(c). One of the main reasons for particle cracking in this cermet  
725 is likely related to the clustering of the alumina inclusions within the microstructure (see Figure 1), which has been shown to influence cracking propensity [157]. In addition, for higher inclusion volume fractions, there are more inter-particle contact points per particle which can increase the stress in a local region of contact point, and, thus, desire for cracking [158]. Moreover, local positive tensile stress generated by inhomogeneous local deformation in the neighborhood of the voids and  
730 observed in the simulations likely contributes to local tensile microcracks that were found to nucleate at preexisting defects (porosity of the matrix).

Another experimentally observed damage micromechanism in the  $\alpha_2(\text{Ti}_3\text{Al})+\gamma(\text{TiAl})$ -submicron grained alumina cermet was the matrix failure due to void deformation and growth. For the failure of the porous matrix, the modified variational formulation of the Gurson model was implemented. The  
735 results (refer to Figure 10) showed that voids tend to grow towards the particle-matrix interface, and this is accompanied by a bulk volume increase (positive strain) because of the fracture porosity in the cavitation matrix. The interfacial debonding is another damage mechanism which was observed experimentally and modeled numerically by implementing polynomial cohesive zone models [105]. A 3D cubic unit cell with interfacial layer between particulates and matrix was pictured in Figure  
740 11. It was shown that there is a debond initiating along the upper half interface of one particle, propagating from left to right along the interface, and then arrest at the location of around  $45^\circ$  from the compression axis. The similar behavior for rate-dependent interfacial decohesion of MMCs has been demonstrated by Zhang et al. [128]. In the current paper, the simulations showed that further increasing the applied strain results in further increases in the maximum equivalent strain and does  
745 not influence the microscopic distribution of deformation. According to the study of fracture in

particulate reinforced MMCs [159], it is recognized that these damage mechanisms are responsible for softening and failure of the composites under dynamic loading.

## 6. Conclusions

This work is aimed at understanding the stress-strain behavior of a  $\alpha_2(\text{Ti}_3\text{Al})+\gamma(\text{TiAl})$ -submicron  
750 grained alumina cermet, considering high particle volume fraction, under high strain rates loading, and accounting for deformation mechanisms (i.e., particle cracking, void deformation and growth, and interfacial debonding). Experiments along with a novel DIC technique was used to measure the global strain fields through the specimen, and the experimentally obtained stress-strain curves were used for the purpose of validating the numerical model. For numerical simulations, the FCC  
755 unit cell model was used for reaching to the high particle volume fraction up to 70% in this cermet. A modified variational formulation of the Gurson model was performed to investigate the effect of damage in the form of porous elastic-plastic matrix void nucleation. By considering different realizations accounting for the experimental variabilities in mechanical properties and microstructure, the model was able to reasonably predict the stiffness, compressive strength, and failure strains from  
760 the experiments. Exploring the material response outside of the experimentally-accessible conditions was allowed by the numerical validated model for the two experimental conditions, thus enabling a more comprehensive understanding on the rate-dependent response of the composite.

The experimentally observed damage micromechanisms such as particle cracking and interface de-  
cohesion (acting as strain-deteriorating parameters), and failure in the matrix by micro-void growth  
765 and coalescence (beneficial for the microstructure in terms of having higher fracture resistance) was also modeled numerically. It was shown that the predicted numerical model was in good agreement with experimental observations in terms of quantitative (e.g., stress-strain curve and compressive behavior) and qualitative (e.g., internal damage behavior) properties of the cermet.

## Acknowledgements

770 This research was sponsored by the Natural Sciences and Engineering Research Council of Canada with support from PRE Labs Inc. and Lumiant Corporation. We thank Calvin Lo and Bernie Faulker for aiding in the completing the experiments.

## References

- [1] K. Rao, Y. Prasad, Processing map and hot working mechanisms in a p/m tial alloy composite with in situ  
775 carbide and silicide dispersions, *Materials science and engineering: a* 527 (24-25) (2010) 6589–6595.

- [2] M. Yamaguchi, H. Inui, K. Ito, High-temperature structural intermetallics, *Acta Materialia* 48 (1) (2000) 307–322.
- [3] X. Wu, Review of alloy and process development of tial alloys, *Intermetallics* 14 (10-11) (2006) 1114–1122.
- [4] R. Imayev, V. Imayev, M. Oehring, F. Appel, Alloy design concepts for refined gamma titanium aluminide based alloys, *Intermetallics* 15 (4) (2007) 451–460.
- 780
- [5] C. Fu, M. Yoo, Interfacial energies in two-phase tial-ti3al alloy, *Scripta materialia* 37 (10) (1997) 1453–1459.
- [6] G. Was, T. Foecke, Deformation and fracture in microlaminates, *Thin Solid Films* 286 (1-2) (1996) 1–31.
- [7] A. Kelly, Composites for the 1990s, *Phil. Trans. R. Soc. Lond. A* 322 (1567) (1987) 409–423.
- [8] Y.-W. Kim, D. M. Dimiduk, Progress in the understanding of gamma titanium aluminides, *JoM* 43 (8) (1991) 40–47.
- 785
- [9] G. Sauthhoff, Multiphase intermetallic alloys for structural applications, *Intermetallics* 8 (9-11) (2000) 1101–1109.
- [10] A. Lasalmonie, Intermetallics: why is it so difficult to introduce them in gas turbine engines?, *Intermetallics* 14 (10-11) (2006) 1123–1129.
- [11] T. Wang, J. Zhang, Thermoanalytical and metallographical investigations on the synthesis of tial3 from elementary powders, *Materials chemistry and physics* 99 (1) (2006) 20–25.
- 790
- [12] C. Koch, Intermetallic matrix composites prepared by mechanical alloying—a review, *Materials Science and Engineering: A* 244 (1) (1998) 39–48.
- [13] K. Kumar, J. Whittenberger, Discontinuously reinforced intermetallic matrix composites via xd synthesis, *Materials science and technology* 8 (4) (1992) 317–330.
- [14] J.-M. Yang, W. Kai, S. Jeng, Development of tic particle-reinforced mosi2 composite, *Scripta metallurgica* 23 (11) (1989) 1953–1958.
- 795
- [15] C. G. Mangin, J. A. Isaacs, J. P. Clark, MMCs for automotive engine applications, *JoM* 48 (2) (1996) 49–51.
- [16] D. Zhang, G. Zhang, Z. LI, The current state and trend of metal matrix composites, *Materials China* 29 (4) (2010) 1–7.
- [17] D. Liu, W. Tuan, Microstructure and thermal conduction properties of Al<sub>2</sub>O<sub>3</sub>-Ag composites, *Acta Materialia* 44 (2) (1996) 813–818.
- 800
- [18] B. Compton, F. Zok, Impact resistance of TiC-based cermets, *International Journal of Impact Engineering* 62 (2013) 75–87.
- [19] M. Karamis, F. Nair, A. Tasdemirci, Analyses of metallurgical behavior of Al–SiCp composites after ballistic impacts, *Composite Structures* 64 (2) (2004) 219–226.
- 805
- [20] H. Chang, J. Binner, R. Higginson, P. Myers, P. Webb, G. King, High strain rate characteristics of 3-3 metal–ceramic interpenetrating composites, *Materials Science and Engineering: A* 528 (6) (2011) 2239–2245.

- [21] V. Verma, B. M. Kumar, Processing of TiCN–WC–Ni/Co cermets via conventional and spark plasma sintering technique, *Transactions of the Indian Institute of Metals* 70 (3) (2017) 843–853.
- 810 [22] W. Wrzesinski, J. Rawers, Self-propagating high-temperature synthesis of tial-sic and tial-al<sub>2</sub>o<sub>3</sub> intermetallic composites, *Journal of Materials Science Letters* 9 (4) (1990) 432–435.
- [23] C. Yeh, S. Su, In situ formation of tial–tib<sub>2</sub> composite by shs, *Journal of alloys and compounds* 407 (1-2) (2006) 150–156.
- [24] R. Ramaseshan, A. Kakitsuji, S. Seshadri, N. Nair, H. Mabuchi, H. Tsuda, T. Matsui, K. Morii, Microstructure and some properties of tial-ti<sub>2</sub>alc composites produced by reactive processing, *Intermetallics* 7 (5) (1999) 571–577.
- 815 [25] D. E. Alman, Reactive sintering of tial–ti<sub>5</sub>si<sub>3</sub> in situ composites, *Intermetallics* 13 (6) (2005) 572–579.
- [26] Z. Li, W. Gao, D. Zhang, Z. Cai, High temperature oxidation behaviour of a tial–al<sub>2</sub>o<sub>3</sub> intermetallic matrix composite, *Corrosion Science* 46 (8) (2004) 1997–2007.
- 820 [27] S. Shu, B. Xing, F. Qiu, S. Jin, Q. Jiang, Comparative study of the compression properties of tial matrix composites reinforced with nano-tib<sub>2</sub> and nano-ti<sub>5</sub>si<sub>3</sub> particles, *Materials Science and Engineering: A* 560 (2013) 596–600.
- [28] S. Shu, F. Qiu, Y. Lin, Y. Wang, J. Wang, Q. Jiang, Effect of b<sub>4</sub>c size on the fabrication and compression properties of in situ tib<sub>2</sub>–ti<sub>2</sub>alc/tial composites, *Journal of Alloys and Compounds* 551 (2013) 88–91.
- 825 [29] S. M. Wiederhorn, L.-S. H. Lum, Structural behavior of ceramics, Tech. rep. (2016).
- [30] M. Anglada, Assessment of mechanical properties of ceramic materials, in: *Advances in Ceramic Biomaterials*, Elsevier, 2017, pp. 83–109.
- [31] M.-S. Suh, Y.-H. Chae, S.-S. Kim, Friction and wear behavior of structural ceramics sliding against zirconia, *Wear* 264 (9-10) (2008) 800–806.
- 830 [32] D. Zhang, Z. Cai, M. Newby, Low cost ti (al/o)/al<sub>2</sub>o<sub>3</sub> and tixaly/al<sub>2</sub>o<sub>3</sub> composites, *Materials Technology* 18 (2) (2003) 94–98.
- [33] N. Travitzky, I. Gotman, N. Claussen, Alumina–ti aluminide interpenetrating composites: microstructure and mechanical properties, *Materials Letters* 57 (22-23) (2003) 3422–3426.
- [34] Z. Cai, D. Zhang, Sintering behaviour and microstructures of ti (al, o)/al<sub>2</sub>o<sub>3</sub>, ti<sub>3</sub>al (o)/al<sub>2</sub>o<sub>3</sub> and tial (o)/al<sub>2</sub>o<sub>3</sub> in situ composites, *Materials Science and Engineering: A* 419 (1-2) (2006) 310–317.
- 835 [35] A. Krell, P. Blank, Grain size dependence of hardness in dense submicrometer alumina, *Journal of the American Ceramic Society* 78 (4) (1995) 1118–1120.
- [36] A. Krell, P. Blank, The influence of shaping method on the grain size dependence of strength in dense submicrometre alumina, *Journal of the European Ceramic Society* 16 (11) (1996) 1189–1200.
- 840 [37] K. Morinaga, T. Torikai, K. Nakagawa, S. Fujino, Fabrication of fine  $\alpha$ -alumina powders by thermal decomposition of ammonium aluminum carbonate hydroxide (aach), *Acta materialia* 48 (18-19) (2000) 4735–4741.

- [38] E. Medvedovski, Ballistic performance of armour ceramics: Influence of design and structure. Part I, *Ceramics International* 36 (7) (2010) 2103–2115.
- [39] J. Chevalier, L. Gremillard, Ceramics for medical applications: A picture for the next 20 years, *Journal of the European Ceramic Society* 29 (7) (2009) 1245–1255.
- [40] L. L. Hench, Bioceramics, a clinical success, *American Ceramic Society Bulletin* 77 (7) (1998) 67–74.
- [41] Y. Wang, J. Lin, Y. He, Y. Wang, G. Chen, Microstructural characteristics of ti-45al-8.5 nb/tib2 composites by powder metallurgy, *Journal of alloys and compounds* 468 (1-2) (2009) 505–511.
- [42] N. Forouzanmehr, F. Karimzadeh, M. Enayati, Study on solid-state reactions of nanocrystalline tial synthesized by mechanical alloying, *Journal of Alloys and Compounds* 471 (1-2) (2009) 93–97.
- [43] W. Zhang, L. Gao, Y. Lei, B. Yang, J. Li, L. Xiao, Y. Yin, Tial/b4c composite fabricated by high energy ball milling and hot press sintering processes and its mechanical properties, *Materials Science and Engineering: A* 527 (27-28) (2010) 7436–7441.
- [44] J. Silvestre, N. Silvestre, J. De Brito, An overview on the improvement of mechanical properties of ceramics nanocomposites, *Journal of Nanomaterials* 2015 (2015) 3.
- [45] M. Estili, A. Kawasaki, H. Sakamoto, Y. Mekuchi, M. Kuno, T. Tsukada, The homogeneous dispersion of surfactantless, slightly disordered, crystalline, multiwalled carbon nanotubes in  $\alpha$ -alumina ceramics for structural reinforcement, *Acta Materialia* 56 (15) (2008) 4070–4079.
- [46] L. Xiang, F. Wang, J. Zhu, X. Wang, Mechanical properties and microstructure of Al<sub>2</sub>O<sub>3</sub>/TiAl in situ composites doped with Cr<sub>2</sub>O<sub>3</sub>, *Materials Science and Engineering: A* 528 (9) (2011) 3337–3341.
- [47] F. Wang, L. Y. Xiang, J. F. Zhu, D. Li, X. F. Wang, Microstructure and mechanical properties of al<sub>2</sub>o<sub>3</sub>/tial in situ composites doped with cr<sub>2</sub>o<sub>3</sub>, in: *Advanced Materials Research*, Vol. 194, Trans Tech Publ, 2011, pp. 1736–1739.
- [48] A. Bartels, H. Clemens, G. Dehm, E. Lach, W. Schillinger, Strain rate dependence of the deformation mechanisms in a fully lamellar  $\gamma$ -tial-based alloy: Dedicated to professor dr. mont. karl leopold maurer on the occasion of his 75th birthday, *Zeitschrift für Metallkunde* 93 (3) (2002) 180–185.
- [49] S. Maloy, G. Gray III, High strain rate deformation of ti48al2nb2cr, *Acta Materialia* 44 (5) (1996) 1741–1756.
- [50] Z. Jin, C. Cady, G. Gray, Y. Kim, Mechanical behavior of a fine-grained duplex  $\gamma$ -tial alloy, *Metallurgical and Materials Transactions A* 31 (13) (2000) 1007–1016.
- [51] S. Osovski, D. Rittel, A. Venkert, The respective influence of microstructural and thermal softening on adiabatic shear localization, *Mechanics of Materials* 56 (2013) 11–22.
- [52] A. Belenky, I. Bar-On, D. Rittel, Static and dynamic fracture of transparent nanograined alumina, *Journal of the Mechanics and Physics of Solids* 58 (4) (2010) 484–501.
- [53] A. Krell, E. Pippel, J. Woltersdorf, W. Burger, Subcritical crack growth in al<sub>2</sub>o<sub>3</sub> with submicron grain size, *Journal of the European Ceramic Society* 23 (1) (2003) 81–89.

- [54] W. Kaplan, D. Rittel, M. Lieberthal, N. Frage, M. Dariel, Static and dynamic mechanical damage mechanisms in tic-1080 steel cermets, *Scripta materialia* 51 (1) (2004) 37–41.
- [55] D. Rittel, N. Frage, M. Dariel, Dynamic mechanical and fracture properties of an infiltrated tic-1080 steel cermet, *International journal of solids and structures* 42 (2) (2005) 697–715.
- 880 [56] Y. Li, K. Ramesh, E. Chin, Comparison of the plastic deformation and failure of a359/sic and 6061-t6/al2o3 metal matrix composites under dynamic tension, *Materials Science and Engineering: A* 371 (1-2) (2004) 359–370.
- [57] E. Pickering, M. O’Masta, H. Wadley, V. Deshpande, Effect of confinement on the static and dynamic indentation response of model ceramic and cermet materials, *International Journal of Impact Engineering* 110 (2017) 123–137.
- 885 [58] Z. Hashin, S. Shtrikman, A variational approach to the theory of the elastic behaviour of multiphase materials, *Journal of the Mechanics and Physics of Solids* 11 (2) (1963) 127–140.
- [59] M. Starink, S. Syngellakis, Shear lag models for discontinuous composites: fibre end stresses and weak interface layers, *Materials Science and Engineering: A* 270 (2) (1999) 270–277.
- 890 [60] P. A. Cundall, O. D. Strack, A discrete numerical model for granular assemblies, *Geotechnique* 29 (1) (1979) 47–65.
- [61] J. Pelletier, P. Sallamand, B. Criqui, Microstructure and mechanical properties of some metal matrix composites produced on different materials by laser cladding, *Lasers in Engineering* 3 (1994) 15–27.
- [62] H. Engqvist, S. Jacobson, N. Axén, A model for the hardness of cemented carbides, *Wear* 252 (5-6) (2002) 384–393.
- 895 [63] N. Shi, M. Bourke, J. Roberts, J. Allison, Phase-stress partition during uniaxial tensile loading of a TiC-particulate-reinforced Al composite, *Metallurgical and Materials Transactions A* 28 (12) (1997) 2741–2753.
- [64] T. Gustafson, P. Panda, G. Song, R. Raj, Influence of microstructural scale on plastic flow behavior of metal matrix composites, *Acta Materialia* 45 (4) (1997) 1633–1643.
- 900 [65] B. N. Legarth, Plasticity dependent damage evolution in composites with strain-gradient effects, *International Journal of Solids and Structures* 63 (2015) 1–10.
- [66] G. Bao, J. Hutchinson, R. McMeeking, Particle reinforcement of ductile matrices against plastic flow and creep, *Acta Metallurgica et Materialia* 39 (8) (1991) 1871–1882.
- [67] R. Hill, A self-consistent mechanics of composite materials, *Journal of the Mechanics and Physics of Solids* 13 (4) (1965) 213–222.
- 905 [68] C.-h. Liu, S. R. Nagel, D. Schecter, S. Coppersmith, S. Majumdar, O. Narayan, T. Witten, Force fluctuations in bead packs, *Science* 269 (5223) (1995) 513–515.
- [69] T. Christman, A. Needleman, S. Suresh, An experimental and numerical study of deformation in metal-ceramic composites, *Acta Metallurgica* 37 (1989) 3029–3050. doi:10.1016/0001-6160(89)90339-8.

- 910 [70] E. Bele, V. S. Deshpande, The compressive response of idealized cermetlike materials, *Journal of Applied Mechanics* 82 (4) (2015) 041009.
- [71] E. Bele, A. Goel, E. Pickering, G. Borstnar, O. Katsamenis, F. Pierron, K. Danas, V. Deshpande, Deformation mechanisms of idealised cermets under multi-axial loading, *Journal of the Mechanics and Physics of Solids* 102 (2017) 80–100.
- 915 [72] K. Ramesh, G. Ravichandran, An ultrasonic evaluation of damage in cermets, in: *Review of Progress in Quantitative Nondestructive Evaluation*, Springer, 1989, pp. 1841–1846.
- [73] L. R. Deobald, A. S. Kobayashi, Dynamic fracture characterization of  $\text{al}_2\text{o}_3$  and  $\text{sicw}/\text{al}_2\text{o}_3$ , *Journal of the American Ceramic Society* 75 (10) (1992) 2867–2870.
- [74] Q. Zhuang, N. Lin, Y. He, X. Kang, Influence of temperature on sintering behavior and properties of tic-fe-co-  
920 ni-cr-mo cermets, *Ceramics International* 43 (17) (2017) 15992–15998.
- [75] B. Amirian, H. Li, J. Hogan, An experimental and numerical study of novel nano-grained ( $\gamma + \alpha_2$ )- $\text{tial}/\text{al}_2\text{o}_3$  cermets, *Materials Science and Engineering: A*.
- [76] K. Madheswaran, S. Sugumar, B. Elamvazhudi, Mechanical characterization of aluminium–boron carbide composites with influence of calcium carbide particles, *International Journal of Emerging Technology and Advanced  
925 Engineering* 5 (7) (2015) 492–496.
- [77] Vic-2D , Correlated Solutions Inc, Irmo, South Carolina.  
URL <http://correlatedsolutions.com/vic-2d/>
- [78] W. Chen, G. Ravichandran, Dynamic compressive failure of a glass ceramic under lateral confinement, *Journal of the Mechanics and Physics of Solids* 45 (8) (1997) 1303–1328.
- 930 [79] W. W. Chen, B. Song, *Split Hopkinson (Kolsky) bar: design, testing and applications*, Springer Science & Business Media, 2010.
- [80] K. Xia, W. Yao, Dynamic rock tests using split hopkinson (kolsky) bar system—a review, *Journal of Rock Mechanics and Geotechnical Engineering* 7 (1) (2015) 27–59.
- [81] K. Ramesh, G. Ravichandran, Dynamic behavior of a boron carbide aluminum cermet: experiments and obser-  
935 vations, *Mechanics of Materials* 10 (1-2) (1990) 19–29.
- [82] H. li, J. Hogan, P. Motamedi, Characterization and mechanical testing on novel ( $\gamma + \alpha_2$ )  $\text{tial}/\text{ti}_3\text{al}/\text{al}_2\text{o}_3$  cermet, *Materials Science and Engineering* [Adoi:10.1016/j.msea.2019.02.039](https://doi.org/10.1016/j.msea.2019.02.039).
- [83] K. Ravichandran, A simple model of deformation behavior of two phase composites, *Acta metallurgica et materialia* 42 (4) (1994) 1113–1123.
- 940 [84] J. Lee, N. J. Kim, J. Jung, E.-S. Lee, S. Ahn, The influence of reinforced particle fracture on strengthening of spray formed cu-tib {sub 2} composite, *Scripta Materialia* 39 (8).
- [85] W. Han, A. Eckschlager, H. J. Böhm, The effects of three-dimensional multi-particle arrangements on the mechanical behavior and damage initiation of particle-reinforced mmcs, *Composites science and technology* 61 (11) (2001) 1581–1590.

- 945 [86] S. Torquato, Random heterogeneous materials: microstructure and macroscopic properties, Vol. 16, Springer Science & Business Media, 2013.
- [87] A. Mbiakop, A. Constantinescu, K. Danas, An analytical model for porous single crystals with ellipsoidal voids, *Journal of the Mechanics and Physics of Solids* 84 (2015) 436–467.
- [88] K. Danas, N. Aravas, Numerical modeling of elasto-plastic porous materials with void shape effects at finite  
950 deformations, *Composites Part B: Engineering* 43 (6) (2012) 2544–2559.
- [89] J. D. Eshelby, The determination of the elastic field of an ellipsoidal inclusion, and related problems, *Proceedings of the Royal Society of London. Series A. Mathematical and Physical Sciences* 241 (1226) (1957) 376–396.
- [90] N. Aravas, P. P. Castañeda, Numerical methods for porous metals with deformation-induced anisotropy, *Computer Methods in Applied Mechanics and Engineering* 193 (36-38) (2004) 3767–3805.
- 955 [91] P. P. Castañeda, The effective mechanical properties of nonlinear isotropic composites, *Journal of the Mechanics and Physics of Solids* 39 (1) (1991) 45–71.
- [92] M. Kailasam, P. P. Castaneda, A general constitutive theory for linear and nonlinear particulate media with microstructure evolution, *Journal of the Mechanics and Physics of Solids* 46 (3) (1998) 427–465.
- [93] K. Danas, P. P. Castañeda, A finite-strain model for anisotropic viscoplastic porous media: I–theory, *European  
960 Journal of Mechanics-A/Solids* 28 (3) (2009) 387–401.
- [94] A. Needleman, On finite element formulations for large elastic–plastic deformations, in: *Advances and Trends in Structures and Dynamics*, Elsevier, 1985, pp. 247–257.
- [95] C. Chu, A. Needleman, Void nucleation effects in biaxially stretched sheets, *Journal of engineering materials and technology* 102 (3) (1980) 249–256.
- 965 [96] V. Tvergaard, A. Needleman, Three dimensional microstructural effects on plane strain ductile crack growth, *International journal of solids and structures* 43 (20) (2006) 6165–6179.
- [97] A. B. Richelsen, V. Tvergaard, Dilatant plasticity or upper bound estimates for porous ductile solids, *Acta Metallurgica et Materialia* 42 (8) (1994) 2561–2577.
- [98] V. Tvergaard, Material failure by void coalescence in localized shear bands, *International Journal of Solids and  
970 Structures* 18 (8) (1982) 659–672.
- [99] K. Jayaraman, K. L. Reifsnider, R. E. Swain, Elastic and thermal effects in the interphase: part ii. comments on modeling studies, *Journal of Composites, Technology and Research* 15 (1) (1993) 14–22.
- [100] J. Kim, Y.-W. Mai, Effects of interfacial coating and temperature on the fracture behaviours of unidirectional kevlar and carbon fibre reinforced epoxy resin composites, *Journal of Materials Science* 26 (17) (1991) 4702–4720.
- 975 [101] A. Miserez, A. Rossoll, A. Mortensen, Fracture of aluminium reinforced with densely packed ceramic particles: link between the local and the total work of fracture, *Acta materialia* 52 (5) (2004) 1337–1351.
- [102] G. I. Barenblatt, The mathematical theory of equilibrium cracks in brittle fracture, in: *Advances in applied mechanics*, Vol. 7, Elsevier, 1962, pp. 55–129.

- [103] G. I. Barenblatt, The formation of equilibrium cracks during brittle fracture. general ideas and hypotheses.  
980 axially-symmetric cracks, *Journal of applied mathematics and mechanics* 23 (3) (1959) 622–636.
- [104] N. Chandra, H. Ghonem, Interfacial mechanics of push-out tests: theory and experiments, *Composites Part A: Applied Science and Manufacturing* 32 (3-4) (2001) 575–584.
- [105] V. Tvergaard, Effect of fibre debonding in a whisker-reinforced metal, *Materials Science and Engineering A* 125 (2) (1990) 203–213, cited By 520. doi:10.1016/0921-5093(90)90170-8.
- 985 [106] C. C. Holland, R. M. McMeeking, The influence of mechanical and microstructural properties on the rate-dependent fracture strength of ceramics in uniaxial compression, *International Journal of Impact Engineering* 81 (2015) 34–49.
- [107] Y. Peng, Q. Wang, L. Ying, M. Kamel, H. Peng, Numerical simulation of dynamic mechanical properties of concrete under uniaxial compression, *Materials* 12 (4) (2019) 643.
- 990 [108] G. Hu, J. Liu, L. Graham-Brady, K. Ramesh, A 3d mechanistic model for brittle materials containing evolving flaw distributions under dynamic multiaxial loading, *Journal of the Mechanics and Physics of Solids* 78 (2015) 269–297.
- [109] F. Appel, J. D. H. Paul, M. Oehring, *Gamma titanium aluminide alloys: science and technology*, John Wiley & Sons, 2011.
- 995 [110] CoorsTek Inc., Advanced alumina brochure, <http://www.coorstek.com/media/1715/advanced-alumina-brochure.pdf> (2016).
- [111] M. Handbook, *Metallic materials and elements for aerospace vehicle structures*, Military Handbook No. MIL-HDBK-5H, Section 5.
- [112] A. H. Tavakoli, P. S. Maram, S. J. Widgeon, J. Rufner, K. Van Benthem, S. Ushakov, S. Sen, A. Navrotsky,  
1000 Amorphous alumina nanoparticles: structure, surface energy, and thermodynamic phase stability, *The Journal of Physical Chemistry C* 117 (33) (2013) 17123–17130.
- [113] A. Bartlett, A. Evans, The effect of reaction products on the fracture resistance of a metal/ceramic interface, *Acta Metallurgica et Materialia* 41 (1993) 497–504. doi:10.1016/0956-7151(93)90078-7.
- [114] M. Güden, O. Akil, A. Tasdemirci, M. Ciftcioglu, I. W. Hall, Effect of strain rate on the compressive mechanical  
1005 behavior of a continuous alumina fiber reinforced ze41a magnesium alloy based composite, *Materials Science and Engineering: A* 425 (1-2) (2006) 145–155.
- [115] D. Zhu, G. Wu, G. Chen, Q. Zhang, Dynamic deformation behavior of a high reinforcement content tib2/al composite at high strain rates, *Materials Science and Engineering: A* 487 (1-2) (2008) 536–540.
- [116] M. J. Kerper, L. E. Mong, M. B. Stiefel, S. F. Holley, Evaluation of tensile, compressive, torsional, transverse,  
1010 and impact tests and correlation of results for brittle cermets, *Journal of Research of the National Bureau of Standards* 61 (3) (1958) 149.
- [117] A. R. Kamali, S. Hadavi, J. Baboee, H. Razavizadeh, Production of TiAl (Ti3Al)/Al2O3 nanocomposite, in: *Journal of Nano Research*, Vol. 3, Trans Tech Publ, 2008, pp. 7–14.

- [118] J. Zhang, H. Di, X. Wang, Y. Cao, J. Zhang, T. Ma, Constitutive analysis of the hot deformation behavior of fe-23mn-2al-0.2 c twinning induced plasticity steel in consideration of strain, *Materials & Design* 44 (2013) 354–364.
- [119] G. Bao, Z. Lin, High strain rate deformation in particle reinforced metal matrix composites, *Acta materialia* 44 (3) (1996) 1011–1019.
- [120] J. Lankford, The influence of temperature and loading rate on flow and fracture of partially stabilized zirconia, *Journal of materials science* 20 (1) (1985) 53–59.
- [121] J. Lankford, Mechanisms responsible for strain-rate-dependent compressive strength in ceramic materials, *Journal of the American Ceramic Society* 64 (2) (1981) C–33.
- [122] S. Acharya, S. Bysakh, V. Parameswaran, A. K. Mukhopadhyay, Deformation and failure of alumina under high strain rate compressive loading, *Ceramics International* 41 (5) (2015) 6793–6801.
- [123] H. Luo, W. Chen, Dynamic compressive response of intact and damaged ad995 alumina, *International Journal of Applied Ceramic Technology* 1 (3) (2004) 254–260.
- [124] J. Pittari III, G. Subhash, J. Zheng, V. Halls, P. Jannotti, The rate-dependent fracture toughness of silicon carbide-and boron carbide-based ceramics, *Journal of the European Ceramic Society* 35 (16) (2015) 4411–4422.
- [125] H. Pouraliakbar, A. H. Monazzah, R. Bagheri, S. S. Reihani, G. Khalaj, A. Nazari, M. Jandaghi, Toughness prediction in functionally graded al6061/sicp composites produced by roll-bonding, *Ceramics International* 40 (6) (2014) 8809–8825.
- [126] S. Fida Hassan, M. Gupta, Development of ductile magnesium composite materials using titanium as reinforcement, *Journal of Alloys and Compounds* 345 (2002) 246–251. doi:10.1016/S0925-8388(02)00413-9.
- [127] P. Pérez, G. Garces, P. Adeva, Mechanical properties of a mg-10 vol. ti composite, *Composites Science and Technology* 64 (2004) 145–151. doi:10.1016/S0266-3538(03)00215-X.
- [128] H. Zhang, K. Ramesh, E. Chin, Effects of interfacial debonding on the rate-dependent response of metal matrix composites, *Acta materialia* 53 (17) (2005) 4687–4700.
- [129] E. Bele, A. Goel, E. Pickering, G. Borstnar, O. Katsamenis, F. Pierron, K. Danas, V. Deshpande, Deformation mechanisms of idealised cermets under multi-axial loading, *Journal of the Mechanics and Physics of Solids* 102 (2017) 80–100. doi:10.1016/j.jmps.2017.01.002.
- [130] M. Tarantino, L. Weber, A. Mortensen, Effect of hydrostatic pressure on flow and deformation in highly reinforced particulate composites, *Acta Materialia* 117 (2016) 345–355. doi:10.1016/j.actamat.2016.06.052.
- [131] M. Taya, H. Lilholt, In *advances in composite materials and structures*, ASME, New York (1986) 21–27.
- [132] D. Zhou, F. Qiu, Q. Jiang, The nano-sized tic particle reinforced al-cu matrix composite with superior tensile ductility, *Materials Science and Engineering: A* 622 (2015) 189–193.
- [133] F. Longy, J. Cagnoux, Plasticity and microcracking in shock-loaded alumina, *Journal of the American Ceramic Society* 72 (6) (1989) 971–979.

- [134] M. Mataya, V. Sackschewsky, Effect of internal heating during hot compression on the stress-strain behavior of alloy 304l, *Metallurgical and Materials Transactions A* 25 (12) (1994) 2737.
- 1050 [135] C. San Marchi, F. Cao, M. Kouzeli, A. Mortensen, Quasistatic and dynamic compression of aluminum-oxide particle reinforced pure aluminum, *Materials Science and Engineering: A* 337 (1-2) (2002) 202–211.
- [136] Z. Tan, B. Pang, D. Qin, J. Shi, B. Gai, The compressive properties of 2024al matrix composites reinforced with high content sic particles at various strain rates, *Materials Science and Engineering: A* 489 (1-2) (2008) 302–309.
- 1055 [137] J. Lankford, The failure of fiber-reinforced ceramic-matrix composites under dynamic loading, *JOM* 47 (5) (1995) 64–68.
- [138] S. Nemat-Nasser, H. Deng, Strain-rate effect on brittle failure in compression, *Acta metallurgica et materialia* 42 (3) (1994) 1013–1024.
- [139] B. Paliwal, K. Ramesh, An interacting micro-crack damage model for failure of brittle materials under compression, *Journal of the Mechanics and Physics of Solids* 56 (3) (2008) 896–923.
- 1060 [140] J. Kimberley, K. Ramesh, N. Daphalapurkar, A scaling law for the dynamic strength of brittle solids, *Acta Materialia* 61 (9) (2013) 3509–3521.
- [141] J. Lankford, Dynamic compressive fracture in fiber-reinforced ceramic matrix composites, *Materials Science and Engineering: A* 107 (1989) 261–268.
- 1065 [142] J. Lankford, High strain rate compression and plastic flow of ceramics, *Journal of materials science letters* 15 (9) (1996) 745–750.
- [143] J. Lankford Jr, The role of dynamic material properties in the performance of ceramic armor, *International Journal of Applied Ceramic Technology* 1 (3) (2004) 205–210.
- [144] C.-C. Perng, J.-R. Hwang, J.-L. Doong, High strain rate tensile properties of an (al<sub>2</sub>o<sub>3</sub> particles)-(al alloy 6061-t6) metal matrix composite, *Materials Science and Engineering: A* 171 (1-2) (1993) 213–221.
- 1070 [145] B. Liu, W. Huang, L. Huang, H. Wang, Size-dependent compression deformation behaviors of high particle content b4c/al composites, *Materials Science and Engineering: A* 534 (2012) 530–535.
- [146] S. Liu, A. Wang, J. Xie, Effect of deformation temperature, strain rate and strain on the strain hardening exponent of copper/aluminum laminated composites, *Advanced Composites Letters* 27 (4) (2018) 096369351802700401.
- 1075 [147] S. Hong, G. Gray, Dynamic mechanical response of a 1060 al/al<sub>2</sub>o<sub>3</sub> composite, *Journal of materials science* 29 (11) (1994) 2987–2992.
- [148] Z. Zhang, D. Chen, Consideration of orowan strengthening effect in particulate-reinforced metal matrix nanocomposites: A model for predicting their yield strength, *Scripta Materialia* 54 (7) (2006) 1321–1326.
- 1080 [149] S. Hong, G. Gray III, J. Lewandowski, Dynamic deformation behavior of al-zn-mg-cu alloy matrix composites reinforced with 20 vol.% sic, *Acta metallurgica et materialia* 41 (8) (1993) 2337–2351.

- [150] L. Bin, W.-m. Huang, H.-w. Wang, M.-l. Wang, X.-f. Li, Compressive behavior of high particle content b4c/al composite at elevated temperature, *Transactions of Nonferrous Metals Society of China* 23 (10) (2013) 2826–2832.
- 1085 [151] Z. Tan, B. Pang, B. Gai, G. Wu, B. Jia, The dynamic mechanical response of sic particulate reinforced 2024 aluminum matrix composites, *Materials Letters* 61 (23-24) (2007) 4606–4609.
- [152] Z. Song, Y. Lu, Mesoscopic analysis of concrete under excessively high strain rate compression and implications on interpretation of test data, *International Journal of Impact Engineering* 46 (2012) 41–55.
- [153] Y. Zhou, Y. Xia, Experimental study of the rate-sensitivity of sicp/al composites and the establishment of a dynamic constitutive equation, *Composites Science and Technology* 60 (2000) 403–410. doi:10.1016/S0266-3538(99)00136-0.
- 1090 [154] I. Tirtom, M. Guden, H. Yilidiz, Simulation of the strain rate sensitive flow behavior of sic-particulate reinforced aluminum metal matrix composites, *Computational Materials Science* 42 (2008) 570–578. doi:10.1016/j.commatsci.2007.09.005.
- 1095 [155] L. Guoju, X. Zhang, Q. Fan, L. Wang, H. Zhang, F. Wang, Y. Wang, Simulation of damage and failure processes of interpenetrating sic/al composites subjected to dynamic compressive loading, *Acta Materialia* 78 (2014) 190–202. doi:10.1016/j.actamat.2014.06.045.
- [156] X. C. Tong, A. K. Ghosh, “fabrication of in situ tic reinforced aluminum matrix composites”, *Journal of Materials Science* 36. doi:10.1023/A:1017946927566.
- 1100 [157] A. Miserez, A. Rossoll, A. Mortensen, Investigation of crack-tip plasticity in high volume fraction particulate metal matrix composites, *Engineering Fracture Mechanics* 71 (2004) 2385–2406. doi:10.1016/j.engfracmech.2004.01.006.
- [158] M. Kouzeli, L. Weber, C. San Marchi, A. Mortensen, Influence of damage on the tensile behaviour of pure aluminium reinforced with  $\zeta = 40$  vol. pct alumina particles, *Acta Materialia* 49. doi:10.1016/S1359-6454(01)00279-8.
- 1105 [159] D. Lloyd, Aspects of fracture in particulate reinforced metal matrix composites, *Acta metallurgica et materialia* 39 (1) (1991) 59–71.